Near steady denudation rates during the late Pleistocene in the tropics

Authors

Etienne Large[1], Julien Charreau[1], Pierre-Henri Blard[1], Germain Bayon[2], Eduardo Garzanti[3], Bernard Dennielou[2], Gwenaël Jouet[2], Alfred Andriamamonjy[4], Amos Fety Michel Rakotondrazafy[4], Aimeryc Shcumacher[1], Laurie Reisberg[1], Natalia Vazquez Riveiros[2], Jacques Giraudeau[5]

[1] : CNRS/Université de Lorraine, UMR 7358 CRPG, 54500 Vandoeuvre-lès-Nancy, France
[2] : CNRS/Université de Bretagne Occidentale/Ifremer, UMR 6538 Géo-Océan, 29280 Plouzané, France
[3] : Università degli Studi di Milano-Bicocca/DISAT, 20126 Milano, Italy
[4] : Université d'Antananarivo/Département des Sciences de La Terre, 101 Antananarivo, Madagascar
[5] : CNRS/Université de Bordeaux, UMR 5805 EPOC, 33615 Pessac, France

Mots:**11742 (without Title, authors, abstract, PLS, key points, key words, text in tables and references)**

Key points

- Paleo-denudation rates of SW Madagascar have remained near-constant and within the range of modern values throughout the past 900 ka.
- Denudation is unaffected by Quaternary climatic cyclicity in the Tropics. Monsoon could be the main control of tropical denudation.
- Turbidites are extremely promising tools for future paleo-denudation rate reconstructions, but need to be better studied and constrained.

Abstract

Denudation is a key parameter controlling the evolution of the Earth's surface, the production of soils, the stability of relief or the long-term evolution of climate. Climate fluctuations conversely have a strong impact on denudation, but these complex feedback mechanisms are still under-constrained. To better predict future changes that will affect our habitat, and understand links between climate and denudation, precise quantification of paleo-denudation rates is required. In this work, we measure cosmogenic radionuclides (^{10}Be) in turbidites of a well-dated marine sedimentary core recovered in the Mozambique Channel to provide a 900 ka long near-continuous record of paleo-denudation rates over the 100 ka climatic cycles. Neodymium isotopes and heavy mineral analysis were used to provide constraints on the provenance of terrigenous sediments exported from Madagascar to the studied site and show that temporal variations in sediment provenance are limited and decoupled from climatic cyclicity. Our ^{10}Be-based paleo-denudation rates are in the same order as modern rates, ranging from 17.4 ± 5.8 mm/ka to 73.9 ± 29.4 mm/ka, and do not show major variations through the Middle and Late Pleistocene. Importantly, we did not identify a systematic significant impact of glacial/interglacial cyclicity on denudation rates. Denudation of this subtropical island may instead have been controlled by variability of monsoon intensity associated with shifts in the Inter Tropical Convergence Zone, but this interpretation remains speculative at this stage as it cannot be recorded within the resolution of cosmogenic-derived denudation rates.

Plain Language Summary

Denudation, the collective action of physical erosion and chemical weathering, is a key parameter controlling the Earth's surface evolution. It is linked to climate by several complex feedback processes. Understanding if, how, and to what extent one controls the other is an active 30 year-long debate in the Earth Science community. In the actual context, understanding how our habitat will react to climate change becomes crucial and precise quantification of past denudation rates is necessary. We reconstruct denudation rates from sediments produced in south-western Madagascar and stored in the Mozambique Channel. Our record spans the last 900 ka, documenting several glacial/interglacial cycles. We also use two proxies to document the evolution of continental sediment sources to the Mozambique Channel. Our results show limited variations of sediment provenance, not following climatic cyclicity over the time considered. Most importantly, we show that the denudation of Madagascar remains constant, within the range of modern values, and completely uncorrelated to any climatic variability over the past 900 ka. We propose that denudation of this tropical island may be controlled by variations of the intensity of monsoons, but this remains a hypothesis as our method does not have the resolution to record such short variations.

Index terms

1616 Climate variability (1635, 3305, 3309, 4215, 4513)
1630 Impacts of global change (1225, 4321)
1815 Erosion
1824 Geomorphology: general (1625)
1862 Sediment transport (4558)

Key words

Geomorphology; Paleo-denudation; Tropics; Turbidite; ^{10}Be; Sediment provenance

1. Introduction

Denudation, the combined effect of chemical weathering and physical erosion, is a key parameter controlling the evolution of the Earth's surface (Portenga and Bierman, 2011). Although tectonic uplift may be an important driver of denudation in some regions (e.g., Godard et al., 2014) we are, in the present work, interested in understanding how climate alone influences denudation. It has often been argued that denudation would be a driver, if not a limiting factor of climatic variations (e.g., West, 2012). Silicate weathering (Berner et al., 1983) and burial of organic carbon (Galy et al., 2007) control atmospheric CO_2 concentrations at geological timescales. Climate in turn, influences denudation rates through the control of precipitation (e.g., Fuller et al., 2009; Moon et al., 2011), temperature and vegetation cover (e.g., Acosta et al., 2015; Olen et al., 2016). The Earth has undergone first-order global climate cooling over the Cenozoic (Zachos et al., 2001), culminating with the onset of the Quaternary glaciations *ca.* 2.56 Ma (Maslin et al., 1996). Understanding and quantifying the feedback processes that exist between climate and denudation, and the extent to which one drives the other has been a key objective, actively debated by Earth scientists over the past 35 years (Hay et al., 1988; Molnar and England, 1990; Zhang et al., 2001). In the current context of global climate change, it is vital to predict how denudation may react to fast high amplitude climate changes. It is therefore essential to understand and quantify how continents erode, both today and under different past climatic conditions.

Past denudation rates have been calculated using various methods (e.g., sedimentary volumes, thermochronology) largely focusing on orogenic settings. A two-fold increase of sedimentation rates since 5 Ma was found in both global marine (Hay et al., 1988) and continental alpine (Kuhlemann et al., 2002) basins. Sediment-budget reconstructions may however be biased by the so-called Sadler effect (Sadler, 1981), lateral shifts of depocenter or stratal discontinuities (Métivier, 2002; Willenbring and Von Blanckenburg, 2010). Detailed sediment volume reconstructions in marine basins based on seismic profiles yielded contradictory results (Clift, 2006), and the signal observed around the Alps could be influenced by the Messinian salinity crisis in the Mediterranean sea. Geochemical proxies such as ^{10}Be/^{9}Be ratios (Willenbring and von Blanckenburg, 2010) showed constant weathering rates since the Late Miocene, although these results do not take into account physical erosion and their integration time has been debated (Von Blanckenburg and Bouchez, 2014). Glacial erosion reconstructions (e.g., Hallet, 1996) suggested the greater effectiveness of glacial versus fluvial erosion implying an increase of erosion rates during glacial periods. Subglacial storage of sediments and their release during deglaciation could however lead to a delay in the rates measured and artificially higher apparent sediment fluxes in Holocene basins (Koppes and Hallet, 2006). Inversion of global thermochronological data showed an up to four-fold increase in exhumation rates during the 0 – 2 Ma period when compared to the 4 – 6 Ma period (Herman et al., 2013), although it was suggested that the spatial gradient in results was associated to local geology of the sampled areas which triggered a biased interpretation (Schildgen et al., 2018).

In addition to these methodological limitations, the theory of global acceleration of denudation relies heavily on the hypothesis that landscape is everywhere in disequilibrium due to oscillating climate (Molnar, 2004). Quantifying denudation rates without these biases and elsewhere than in tectonically active, glaciated, and mountainous regions is therefore key. Cosmogenic nuclides in the tropics may thus prove crucial to better addressing the debate. In this work, using cosmogenic nuclides measured in turbidites at a tropical latitude and under quiescent tectonic settings, we provide new information to help understand how denudation responds to climatic forcings on the scale of glacial cycles (10 ka) and of the Pleistocene.

Cosmogenic nuclides and especially *in-situ* ^{10}Be measured in river sediments are powerful tools for reconstructing basin averaged denudation rates (Brown et al., 1995) with the advantages of being widely used and known (e.g., Granger et al., 1996; Portenga and Bierman, 2011), and unaffected by changes in depocenter or incomplete sediment preservation. *In-situ* cosmogenic nuclides in sedimentary records allow determination of paleo-denudation rates (e.g., Marshall et al., 2017; Puchol et al., 2017), an approach applied to a number of different archives such as cave sediments (e.g., Haeuselmann et al., 2007), lake deposits (e.g., Garcin et al., 2017), foreland fluvial deposits (Charreau et al., 2011) or turbidite records in marine sediment cores (e.g., Mariotti et al., 2021).

Many of these studies were focused on tectonically active (e.g., Gonzalez et al., 2016) or previously glaciated regions (e.g., Grischott et al., 2017; Madella et al., 2018, Mariotti et al., 2021). Over long time scales up to 10 Ma, paleo-denudation records may also have been influenced by changes in geodynamic forcing and elevation changes (e.g., Lenard et al., 2020; Puchol et al., 2017). Over shorter Quaternary time scales, paleo-denudation rates were reconstructed in various geological settings (Bekaddour et al., 2014; Fisher et al., 2023; Fuller et al., 2009; Grischott et al., 2017; Hidy et al., 2014; Mariotti et al., 2021; Marshall et al., 2017; Schaller et al., 2002) but few records display sufficient continuity and resolution to reveal the impact of climate oscillations (Fisher et al., 2023; Mariotti et al., 2021; Marshall et al., 2017).

In the southern Central Andes, Fisher et al. (2023) showed synchronicity between variations in denudation rates and Milankovitch-driven, 400-ka eccentricity cycles. In Oregon, Marshall et al. (2017) also proposed that climate modulates erosion rates over a glacial-interglacial time scale. Both studies were carried out in glaciated or periglacial regions. Conversely, the analysis of ^{10}Be in turbidites deposited in the Var submarine sedimentary system (France, Southern Alps) allowed Mariotti et al. (2021) to reconstruct a 75 ka record of paleo-denudation rates non-linearly responding to climatic forcing with rates estimated to be 2-7 times higher during the Last Glacial Maximum (LGM) than during previous minor glacial periods. Such a non-linear response of denudation to climate change is plausibly controlled by the interplay between glacier velocity and basin topography. The link between Quaternary climatic oscillations and denudation in non-glaciated areas remains, however, obscure and requires more observations.

The present work aims at filling this knowledge gap by focusing on sediments generated in SW Madagascar, a sub-tropical island which remained unglaciated and tectonically quiescent through the Quaternary. In Madagascar, modern denudation rates are believed to be closely linked to the presence of gullies, locally referred to as lavakas (Brosens et al., 2022) which may have increased in the last 1 ka due to anthropogenic forcings (settlements, deforestation and cattle grazing). The physical mechanisms related to the formation of these lavakas and their impact on sediment generation however remain unclear. ^{10}Be-derived denudation rates of the lavakas yield values of 3.2 ± 0.2 to 19.7 ± 1.2 mm/ka (Cox et al., 2009). Paleo-denudation rate determination for Madagascar are limited to two > 1 ka old river terrace samples (Cox et al., 2009), which yielded similar denudation rates (11.1 ± 1.4 mm/ka and 12.4 ± 1.6 mm/ka) to those of modern rivers and active lavakas, suggesting a long term control of denudation rates by lavakas, and a possibly limited effect of anthropogenic activities.

In the present work, we use quartz grains from the turbiditic layers of a 26-m-long marine sedimentary piston core retrieved offshore western Madagascar recording sediments with ages between ~12 ka and 900 ka to measure paleo-denudation rates up to the Mid Pleistocene Transition (MPT) that occurred between 1.2 and 0.7 Ma when the frequency of glacial/interglacial cycles changed from 100 ka to 40 ka (Berends et al., 2021). These analyses were supplemented by the acquisition of new ^{10}Be-derived denudation rates for five modern river catchments in SW Madagascar, together with neodymium isotopes and heavy mineral analyses of corresponding samples to investigate the potential effect of changing sediment provenance on calculated denudation rates.

2. Study Area

2.1. *Physiography of Madagascar*

Madagascar is a tropical to sub-tropical island located offshore southern Africa to the east of the Mozambique Channel (11.9°S to 25.6°S). Three main topographic zones are identified: a large central plateau with limited relief (mean elevation of ~1200 m) but with some high points (e.g., Mount Maromokotro, 2876 m) flanked by two zones of lower altitude (Fig.1A). The western transition from the central plateau down to the sea corresponds to a series of cuestas (ridges with gentle slopes), formed by differential erosion of hard and soft layers (Delaunay, 2018). To the east, the great escarpment separates the high plateau from the narrow (50-190 km) coastal plain, extending for 1500 km from north to south and containing several small independent basins (Wang et al., 2021). The drainage divide between eastern and western watersheds is located only 50-100 km away from the eastern coast, reflecting the strong asymmetry of the relief, with much steeper slopes in the east than in the west. Major drainage basins drain towards the Mozambique Channel in the west, while rivers debouching into the open Indian Ocean are short and tend to extend westward by headward erosion and drainage capture

(Fig. 2). Two main sedimentary basins exist in the western part of the island, the Morondava basin to the south of Cap Saint-André and the Mahajanga basin to the north, spreading over~ 9000 km^2 and ~13,000 km^2, respectively (Fig. 1A).

2.2. *Geologic domains of Madagascar*

The geology of Madagascar comprises two main regions: a widespread sedimentary zone in the western part and Mesoarchean to Neoproterozoic crystalline basement in the central and eastern parts (Boger et al., 2019). Mostly metamorphic basement rocks include granitoids, schists, mafic gneisses (Tucker et al., 2014), high-grade metasediments, (Archibald et al., 2015), amphibolites and dolomitic marbles (Cox et al., 1998; Tucker et al., 2011), and are intruded by Neoarchean granites (Paquette et al., 2003; Tucker et al., 2011) such as the Tonian plutonic suite of Imorona-Itsindro (Archibald et al., 2017) and the Ambalavao (Archibald et al., 2019) and Manambato suites (Thomas et al., 2009) (Fig. 1B). The Morondava and Mahajanga basins in the west contain up to 10-km-thick Carboniferous to Neogene sedimentary successions (Besairie, 1972; Delaunay, 2018) (Fig.1B) including continental siliciclastic sediments and shallow-marine carbonate shelf deposits (Andriampenomanana et al., 2017). In the rest of the island, Cenozoic sediments fill small interior basins (e.g., Aloatra Lake and Ranotsara plains; Fig.1B) and a narrow strip of Quaternary deposits lines the eastern coast. The geology of Madagascar was summarized in a geological map from Roig et al. (2012).

2.3. *Tectonic activity of Madagascar*

Although Madagascar is considered as tectonically dormant, over the past 15 Ma, large-wavelength uplift of 1-2 km was revealed by inverting 98 river profiles throughout the island (Roberts et al., 2012). Rates of general uplift, widespread throughout the island, reach 0.2 to 0.4 mm/a and are attributed to Neogene convective mantle upwelling below the island. Widespread uplift, however may have remained active only until the end of the Miocene (Delaunay, 2018). The topography of central Madagascar, where the crust appears to be thinner, is held to be maintained by dynamic topography and upwelling of hot mantle material (Paul and Eakin, 2017; Pratt et al., 2017). Active uplift, very localized to the northern tip of Madagascar, was also revealed by the study of elevated marine terraces (Stephenson et al., 2019). Volcanism as recent as Late Pleistocene is also recorded to the northwest and southwest of the Ankaratra volcanic complex (Fig.1) (Melluso et al., 2018; Rufer et al., 2014).

2.4. *Climate*

Madagascar is located at the southern limit of the modern Inter Tropical Convergence Zone (ITCZ), where converging winds and maximum precipitation are associated to the ascending branch of the Hadley circulation (e.g., Hu et al., 2007), convective cells bringing warm moist air into the upper troposphere and cold dry air down to mid latitudes, their lower part being the trade winds. The seasonal migration of the ITCZ drives a monsoon climate in Madagascar (e.g., Gadgil, 2018), especially in the southwest, with seasonal and spatial variability in precipitation marked by wet (December to February) and dry (March to November) seasons. In Tulear for instance (Fig. 1A and 2) wet and dry periods correspond respectively to up to ~ 200 mm/month and down to ~ 10 mm/month of precipitation. Due to the moisture brought by the trade winds and to the N/S striking reliefs, a strong orographic effect produces a marked decreasing precipitation gradient from East to West (Fig. 1A). Ecosystems thus vary markedly across the island. The eastern coastal plains and the northernmost parts of the island are covered by humid forests whereas the western and southwestern forests are mainly dry, spiny, or subhumid. The central plateau is characterized by a grassland-woodland mosaic and mangroves are found along the western and northwestern coasts (Antonelli et al., 2022). Because of such climatic conditions, much of Madagascar is covered by lateritic soils, up to 25-m-thick in the southern parts of the island (Paul et al., 2022).

3. Material

To compare paleo-denudation rates with modern denudation rates, and to determine source signatures for detrital Nd in modern Malagasy rivers, ~ 2 kg of river sediments were sampled from active bars of the Mangoky, Tsiribihina, Onilahy, Manambolo and Morondava rivers (Fig. 2, Table 2).

For paleo-provenance analysis and calculation of ^{10}Be-derived paleo-denudation rates, sand fractions were sampled on turbidites from the 26.42 m long MOZ4-CS24 sedimentary core at the Ifremer facility in Brest (France). This core was recovered by a CALYPSO piston corer on the RV "Pourquoi pas ?" in 2015 during the PAMELA-MOZ4 cruise (Jouet and Deville, 2015) which was part of the PAMELA (Passive Margins Exploration LAboratories) project. The core, retrieved ~150 km of SW of Madagascar on net-depositional areas called terraces overhanging the axis of the Tsiribihina submarine canyon at 3090 m water depth (Fig.2), consists of hemipelagic carbonated ooze intercalated with 99 turbiditic sand layers ranging in thickness from 0.5 to 19.5 cm (Fig. 3A). Seventeen turbidite layers were sampled based on grain size, representativity and availability (typical weight of turbiditic samples ~ 35 g, Fig. 3B). The chronostratigraphy is based on the fluctuations of ^{18}O/^{16}O (∂^{18}O hereafter, expressed in ‰ vs. Vienna Pee-Dee Belemnite, VPDB, relative to NSB-19) measured in tests of the epibenthic benthic foraminiferal species *Cibides Wuellestorfi* and bio-stratigraphic analyses of calcareous nannofossil assemblages. These were studied in the hemipelagic intervals immediately surrounding the turbidite deposits considered as instantaneous events (i.e., same age at base and top of a turbidite). The δ^{18}O measurements were analyzed at the Leibniz Laboratory for Radiometric Dating and Stable Isotope Research at Kiel University, Germany, using a Kiel IV carbonate preparation device connected to a ThermoScientific MAT 253 mass spectrometer. Precision of all different laboratory internal and international standards (NBS-19 and IAEA-603) is ± 0.09 ‰. The preliminary age model was constructed by correlating ∂^{18}O variations to the LR04 benthic stack (Lisiecki and Raymo, 2005) with the program AnalySeries (Paillard et al., 1996), and then confirmed by calcareous nannofossil assemblages of stratigraphic significance (Fig. 3C, Sup. Info. 1). Isotopic tie points and calcareous nannofossil data (Sup. Info. 1, 2 and 3) are presented in supplementary material. The combined datasets indicate that the stratigraphic range of core MOZ4-CS24 extends from Holocene (11.6 ka) to Mid Pleistocene (905 ka), corresponding to Marine Isotope Stages (MIS) 1 to the MIS 22-23 boundary, and that the sedimentation is discontinuous with a ca. 200ka hiatus identified between MIS11 and MIS 15 (from 421 ka to 599 ka). Further information is provided in supplementary materials (Sup. Info. 1 and 2).

4. Methods

4.1. *Cosmogenic radionuclide denudation rates*

Paleo-denudation rates in Madagascar, were calculated following a method extensively described in previous studies (e.g., Charreau et al., 2021; Puchol et al., 2017). We measured the bulk ^{10}Be concentrations in quartz grains N_{total} in $at.g^{-1}$ of the sampled turbiditic layers from MOZ4-CS24 core. The basin-averaged denudation rate $\bar{\varepsilon}$ was then calculated from N_{total} by solving the following equation 1 (e.g., Charreau et al., 2011; Puchol et al., 2017):

$$N_{total} = e^{-\lambda t}\left[\sum_{j=1:3}\frac{\overline{P_j}}{\frac{\bar{\varepsilon}\,\rho_r}{\Lambda_j}} + N_{fp}\right] \quad (1)$$

where $\overline{P_j}$ is the overall paleo-production rate of ^{10}Be averaged over the drainage basin at the time of erosion, which accounts for all cosmogenic-production mechanisms (spallation, ‘n’, and slow and fast muons, ‘µs’ and ‘µf’, respectively, indicated by j = 1:3), ρ_r is the density of the denuded rocks (taken as 2.6 g/cm^3), λ the radioactive decay constant (^{10}Be half-life is 1.387 Ma, Korschinek et al., 2010), Λ_j the characteristic attenuation lengths of cosmogenic-production mechanisms (Λ_n = 160 g/cm^2, $\Lambda_{\mu s}$ = 1500 g/cm^2, and $\Lambda_{\mu f}$ = 4320 g/cm^2, Braucher et al., 2011), and t the time at which the sediments were buried (i.e. depositional age). N_{fp} is the number of ^{10}Be atoms (per g of quartz) accumulated by sediments during transport across the onshore watershed.

To solve equation 1 and derive paleo-denudation rates from measured ^{10}Be concentrations, assumptions and corrections must be made (Charreau et al., 2021, 2011; Puchol et al., 2017). Firstly, we assumed paleo-production rates equivalent to modern basin averaged cosmogenic ^{10}Be production rates. Cosmogenic nuclides being produced by cosmic rays, their production is dependent on altitude (amount of atmosphere blocking the cosmic rays) and latitude (orientation and strength of the geo-magnetic field) (Dunai, 2000). Assuming a relative tectonic quiescence of Madagascar allowed us to consider that no significant change in the elevation of the drained watersheds had occurred since 900 ka, although drainage basin reorganizations may have taken place. This possibility was checked by comparing the Nd isotopic compositions ($^{143}Nd/^{144}Nd$ ratio, or εNd using the epsilon notation) and heavy mineral data throughout the MOZ4-CS24 core with modern sand samples (see below). Production rates of ^{10}Be were calculated using the Basinga ArcGIS toolbox (Charreau et al., 2019). Based on a Digital Elevation Model (DEM), this program calculates a production rate integrated over an entire drainage basin by determining a rate for each pixel of the DEM depending on its latitude and elevation.

Secondly, because cosmogenic ^{10}Be concentrations are measured in quartz grains, we assumed that quartz was representative of basin lithology. Areas of quartz-bearing lithologies (alluvial and lake deposits, basement rocks, quartzites, sandstones and unconsolidated sands, Fig. 1B) were thus isolated for production calculations (Fig. 2). These lithologies are widespread in the central high plateaus and in the western drainage basins, representing ~85 % of the total drainage area considered in this study. Although these lithologies do not necessarily erode at the same rates, cosmogenic nuclides measured in river sands at the outlet of the drainage allow to calculate a basin-integrated mean denudation rate.

For paleo-denudation rate calculations (Tab. 1), we assumed that core turbiditic sediments were sourced from all considered basins. We hence used the production rate of the entire quartz rich area shown in yellow in figure 2, corresponding to values of 4.798 at/g/a, 0.041 at/g/a and 0.015 at/g/a for neutrons, fast muons and slow muons, respectively. Modern denudation rates were calculated using the production rates of the area of quartz-bearing lithologies within each basin (results are given in table 2). All production rates were corrected for topographic shielding using relief shadow modelling from (Codilean, 2006).

Thirdly, we assumed that ^{10}Be production during transport until final deposition was negligeable, as discussed below. To solve equation 1 and assess the associated errors on paleo-denudation rates, we used a Montecarlo simulation, as described in Puchol et al. (2017), which conservatively explores the range of each input parameter with 10^4 draws.

To each denudation rate data, an integration time (or characteristic time) is associated (tables 1 and 3). It corresponds to the time over which the denudation rate calculated is valid, in other words, the time taken by a quartz mineral to cross the subsurface depth where it accumulated cosmogenic nuclides (usually 60 cm). Denudation rates of 50 mm/ka will have an integration time of 12 ka, (60 cm / 0.005 cm/a, see Von Blanckenburg, 2005 for further explanation).

4.2. *Sample treatment for* in situ *cosmogenic ^{10}Be analysis*

Turbidite samples were wet-sieved at 50 µm, 100 µm and 250 µm, depending on the general granulometry of the turbidites and the availability of these fractions (Fig. 3A). Following Mariotti et al. (2019) and to ensure that cosmogenic concentration in the finer fraction of turbidite sands (50-100 µm) and in the coarser fraction of modern-river sands (usually > 100 µm) were compatible, we preliminarily tested the finer 50-100 µm and coarser 100-250 µm fractions of 2 core samples. Results showed significant differences in ^{10}Be concentrations for sample S16 1559-1562 and differences within uncertainties for sample S21 2060-2062 (Table 1). For both samples, ^{10}Be was extracted from the finer grained fraction in the former, ancient lab of CRPG (see below) while chemical separation of the coarser fractions was done in a newly constructed clean lab facility. Thus, the confidence on these two fine grained samples is lower. Following Mariotti et al. (2019) and because the size of the core samples left us no other option, we decided to work with the 50 - 250 µm fraction whenever possible.

Modern river sands were wet sieved at 100 µm to 700 µm. To minimize size-related differences with core data, the Tsiribihina, Mangoky and Onilahy samples (Fig.2) were additionally measured on the 50-250 µm fraction to check for any discrepancies in results. Only the Onilahy sample showed significant differences in ^{10}Be concentrations between the two fractions (100-700 µm and 50-250 µm, Tab. 3).

The non-magnetic fraction of sieved sands was separated using a Frantz magnetic separator following Rosenblum (1958) and purified using a method modified from Kohl and Nishiizumi (1992). Sands were leached with HCl 36% (i.e., concentrated HCl) to dissolve carbonate and organic matter, before applying three to seven rounds of ~200 mL of 1/3 HCl 36%, 2/3 H_2SIF_6 41% solution to obtain pure quartz. Quartz grains were etched using three rounds of HF 48% (i.e., concentrated HF) to dissolve ~ 30% of each grain and remove the atmospheric ^{10}Be variety incorporated in the outer rim of the grains (Brown et al., 1991). Once purified, chromatographic column chemistry (first with an anionic resin DOWEX 1x8 and HCl 10.2 mol/L, then a cationic resin DOWEX 50Wx8 with HCl 1 mol/L) was done to extract BeO.

Samples were prepared in different batches. The first batch (batch 1 in Table 1) was treated in the old CRPG lab with a phenakite spike from CRPG with ^{9}Be concentration of 2020 ± 83 (Tab. 4). The second batch was treated at CEREGE (batch 2 in Table 1) with the CERGE spike with ^{9}Be concentration of 3025 ± 9 (Tab. 4). The last four batches were treated in a new clean lab at CRPG (batches 3 – 4 in Table 1, and batches 5 – 6 of Table 3) with a new spike developed at CRPG with ^{9}Be concentration of 2129 ± 13 ppm (Tab. 4). $^{10}Be/^{9}Be$ ratios were then measured at the ASTER facility in CEREGE, Aix-en-Provence (France). The Accelerated Mass Spectrometer (AMS) was calibrated using the STD-11 in-house standard (Braucher et al., 2015), with a certified $^{10}Be/^{9}Be$ ratio of $5.67622 \pm 1.09551 \times 10^{-12}$, similar to KNSTD07 standardization (Nishiizumi et al., 2007).

Mean analytical $^{10}Be/^{9}Be$ blank ratios are of $1.13 \pm 0.234 \times 10^{-15}$. However, these blanks are higher for batches 1 and 2 ($4.2 \pm 0.513 \times 10^{-15}$ and $2.2 \pm 0.379 \times 10^{-15}$, Table 4) than for batches 3 to 6 ($1.7 \pm 1.3 \times 10^{-16}$ to $11.8 \pm 2.6 \times 10^{-16}$, Tab. 4) as expected due to the change to a new CRPG clean lab and a newly created ^{9}Be spike.

4.3. *Geochemical analyses*

Sediments reaching the Tsiribihina turbiditic system are provided not only by the Tsirbihina, but also by all continental basins considered in this study (Fig.2). Relative provenance of these sediments may evolve through time, thus affecting the concentration of cosmogenic nuclides and calculations of paleo-denudation rates. To address this issue we used Nd isotopes, or more exactly, variations in the abundance of the radiogenic isotope ^{143}Nd, formed by the decay of ^{147}Sm, normalized to the abundance of the non-radiogenic isotope ^{144}Nd. Unlike stable isotope tracers, abundances of the radiogenic isotope ^{143}Nd are not directly affected by weathering processes, making Nd isotopes a particularly robust tool for source tracing (e.g., Bayon et al., 2015; Garzanti et al., 2022b). Furthermore, because of the very long half-life of ^{147}Sm (~106 Ga), the ^{143}Nd/^{144}Nd ratios of the sediment sources can be viewed as essentially constant over the < 1 Ma time period covered by this study. Variations in Nd isotopic composition are often expressed in εNd units, which represent the deviation, in parts per 10^4, of the measured ^{143}Nd/^{144}Nd ratio from the assumed value of a chondritic uniformed reservoir (CHUR, ^{143}Nd/^{144}Nd = 0.51263 Bouvier et al., 2008). Source regions with different Sm/Nd ratios will develop different ^{143}Nd/^{144}Nd ratios, and thus different εNd values, over time. The old Precambrian basement rocks of the central plateau in Madagascar drained by Manambolo and Mangoky rivers (Fig. 1B) are characteristically associated with highly negative sediment εNd signatures of -17 to -24, respectively (Garzanti et al., 2022b), a range of values which can be used to track significant changes in sediment sources to the studied underwater Tsiribihina valley terrigenous sedimentary record. Nd isotope data in Garzanti et al. (2022b) were obtained from the same 15-500 µm fraction analyzed for heavy minerals. In this study, εNd values were determined on the same 50-250 µm fraction used for ^{10}Be measurements, for 15 turbiditic samples and 5 river sand samples (Fig. 2, Tab. 5). To assess any potential grain-size effects, we also measured the separate 50-100 µm and 100-250 µm size fractions in the five river sand samples and on turbidite samples whenever possible (3 samples were measured on the 50-100 µm fraction alone, 4 on the 100-250 µm fraction alone, and 8 were measured on both fractions, Tab. 5).

All samples were sieved and passed through a Frantz magnetic separator. The MOZ4-CS24 core sample chemical preparation was performed at Ifremer, Brest, following the methods described in Bayon et al. (2009, 2015). This involves successive leaching of the sieved sample fractions in 5% acetic acid, 15% acetic acid mixed with 0.05M hydroxylamine hydrochloride, and 5% hydrogen peroxide, to remove carbonates, Fe-Mn oxyhydroxides, and organic material, respectively. After careful rinsing and drying, residues were then digested by alkaline fusion prior to separation of Nd using standard column chromatography techniques employing AG50W-X8 and Ln Spec resins. Isotopic measurements were made on the Neptune MC-ICP-MS at the Pôle Spectrométrie Océan (Brest). Modern river sands were processed in CRPG in a newly constructed clean lab facility using the same leaching and chemical separation methods, but with no alkaline fusion. Alkaline fusion is no longer integrated in the typical sample processing protocol of CRPG, as its effect has proven to be minor. Isotopic measurements were made on the Thermofischer Neptune Plus MC-ICP-MS of the CRPG. In both laboratories, corrections for mass bias on Nd isotope measurements were made using the exponential law with ^{146}Nd/^{144}Nd = 0.7219. Replicate measurements of JNdi-1 standard solutions gave a ratio of ^{143}Nd/^{144}Nd = 0.512110 ± 0.000025 (2 s.d.; n=10) at Ifremer and ^{143}Nd/^{144}Nd = 0.512098 ± 0.000011 at CRPG. To agree with the reference value (0.512115; Tanaka et al., 2000), CRPG values were multiplied by a correction factor of

1.000033566. All samples were then normalized to the CHUR value of $^{143}Nd/^{144}Nd$ = 0.512630 (Bouvier et al., 2008).

Major and trace element compositions were determined on bulk-sediment core samples and on separate size fractions of leached river-sand samples by the SARM (Service d'Analyse des Roches et des Minéraux, https://sarm.cnrs.fr/index.html/). Additionally, abundances for selected major and trace elements on the detrital sediment fractions of core MOZ4-CS24 were also determined at the Pôle Spectrométrie Océan (Brest) using an Element XR ICPMS instrument (Sup. Info. 7).

4.4. *Heavy minerals*

As an additional approach to source tracing, heavy-mineral analyses for the 17 sediment samples from MOZ4-CS24 core were performed at the Laboratory for Provenance Studies (University of Milano-Bicocca, Italy). Quartered aliquots of each bulk sediment sample (ca. 3-4 g) were wet sieved with a standard 500 µm sieve in steel and with handmade tissue-net sieves with 15 µm mesh. Heavy minerals were separated from the 15-500 µm fraction by centrifuging in sodium polytungstate (density 2.90 g/cm^3) and recovered by partial freezing with liquid nitrogen. An appropriate amount of the dense fraction was split carefully with a micro-riffle box and mounted with Canada balsam (n = 1.54) on a glass slide. Under a polarizing microscope, ≥ 200 transparent heavy minerals were point-counted at a suitable regular spacing to minimize overestimation of smaller grains (Garzanti and Andò, 2019). All uncertainly determined grains were checked and properly identified in a wide spectral range (140 - 4200 cm^{-1}) by an inVia™ Renishaw Raman spectrometer equipped with a green laser 532 nm and a 50x LWD objective according to Andò and Garzanti (2014). Heavy-mineral concentration was calculated as the volume percentage of total (HMC) and transparent (tHMC) heavy minerals (Garzanti and Andò, 2007). The ZTR index is the sum of zircon, tourmaline and rutile over total transparent heavy minerals (Hubert, 1962) and is classically used to estimate the "durability" (i.e., the extent of recycling; Garzanti, 2017) of the assemblage. The "Amphibole Colour Index" ACI and "Metasedimentary Minerals Index" MMI are used to estimate the average metamorphic grade of metaigneous and metasedimentary source rocks, respectively. They vary from 0 in detritus from low-grade rocks yielding exclusively blue/green amphibole and chloritoid, to 100 in detritus from high-grade rocks yielding exclusively brown hornblende and sillimanite. The "Sillimanite Index" Sil.I., defined as the ratio between prismatic sillimanite and total (prismatic + fibrolitic) sillimanite grains, varies from 0 in detritus from upper amphibolite-facies metasediments to 100 in detritus from granulite-facies metasediments (Andò et al., 2014). Significant minerals are listed in order of abundance below.

5. Results

5.1. *^{10}Be concentrations and paleo-denudation rates*

Measured $^{10}Be/^{9}Be$ ratios range from 2.6 ± 0.3 10^{-15} to 19.6 ± 1.0 10^{-15} with a mean of 6.5 ± 0.3 10^{-15} (Mean Square of the Weighted Deviates (MSWD) 63, p 0, calculated using http://isoplotr.es.ucl.ac.uk, Vermeesch, 2018) for turbidite samples and from 5.9 ± 0.2 10^{-14} to 21.6 ± 0.6 10^{-14} with a mean of 7.6 ± 0.2 10^{-14} (MSWD 43, p 0) for modern sands. Accordingly, the measured concentrations of ^{10}Be in turbidite samples, corrected from blank values, but uncorrected for radioactive decay range from 4.4 ± 1.8 10^{4} at/g at 615 ka to 19.9 ± 5.3 10^{4} at/g at 136 ka (Tab. 1), with a mean of 8.0 ± 0.4 10^{4} at/g (MSWD 7.2, p 0). For modern river sand samples, somewhat higher concentrations range from 8.3 ± 0.6 10^{4} at/g for the Morondava river to 34.1 ± 1.1 10^{4} at/g for the fine-grained Tsiribihina sample, with a mean of 16.5 ± 0.4 10^{4} at/g (MSWD 130, p 0). Complete raw cosmogenic ^{10}Be dataset is given in tables 1 and 3.

Calculated paleo-denudation rates range from 20.9 ± 4.6 mm/ka at 637 ka to 73.9 ± 29.4 mm/ka at 615 ka (Fig. 4A) with a weighted mean average of 27 ± 3 mm/ka (MSWD 0.81, p 0.7). Samples stratigraphically below the hiatus (i.e., during the MPT) yield mean denudation rates of 24.9 ± 4.7 mm/ka (MSWD 0.5, p 0.8), whereas samples above (i.e., after the MPT) yield mean denudation rates of 28.0 ± 3.9 mm/ka (MSWD 1.0, p 0.5).

Modern denudation rates in main SW Madagascar catchments (Fig. 2, Tables 2 and 3) range from 11.2 ± 2.3 mm/ka for the Tsiribihina river to 30.4 ± 6.5 mm/ka for the Morondava river, with a weighted mean of 15.7 ± 2.4 mm/ka (MSWD 3, p 4 10^{-3}). The highest denudation rates thus characterize the smallest basin (Tables 2 and 3). Weighted mean denudation rates are 14.8 ± 3.1 mm/ka (MSWD 2.2, p 0.091) for finer fractions (50-250 µm) and 17.1 ± 3.8 mm/ka (MSWD 4.3, p 0.0047) for coarser fractions (100-700 µm). Such a discrepancy is accounted for by the notably different values obtained for different fractions for the Onilahy river alone (15.1 ± 3.1 mm/ka and 25.7 ± 5.4 mm/ka for the finer and coarser fractions respectively, Tab. 3), which could be explained by fine grained aeolian deposits found in the more arid parts of the island (the southwestern-most areas), that could contaminate river sands leading to higher ^{10}Be concentrations in the finer fractions. Because we have no quantification of this aeolian input, we hereafter use the weighted mean value of the two fractions for the Onilahy river (17.7 ± 5.3 mm/ka, Fig 2). The Mangoky (21.1 ± 4.4 mm/ka and 23.7 ± 4.9 mm/ka for the finer and coarser fractions respectively, Tab. 3) and Tsiribihina (11.2 ± 2.3 mm/ka and 12.0 ± 2.4 mm/ka for the finer and coarser fractions respectively, Tab. 3) samples do not show any statistically relevant difference between size fractions.

5.2. *Provenance analysis*

Nd isotope data for turbidite samples range between εNd -15.6 ± 0.2 and -19.5 ± 0.2 (Table 5, Fig. 4B) with a weighted mean of -16.8 ± 0.15 (MSWD 5.4, p 2.6 10^{-15}). Samples analyzed in two different size fractions yield weighted mean εNd values of -16.3 ± 0.2 (MSWD 2.6, p 5.6 10^{-3}) for the finer 50-100 µm fraction, and -16.9 ± 0.2 (MSWD 2.7, p 2.2 10^{-3}) for the coarser 100-250 µm fraction. Finer and coarser fractions yield mean εNd values of -16.9 ± 0.3 (MSWD 8.8, p 4.2 10^{-7}) and -16.5 ± 0.3 (MSWD

0.65, p 0.63) above the hiatus and -16.2 ± 0.3 (MSWD 3.1, p 9 10^{-3}) and -17.49 ± 0.8 (MSWD 4.4, p 2 10^{-4}) below the hiatus, respectively.

The Nd isotopic composition of modern river sand samples ranges between -15.8 ± 0.3 and -20.5 ± 0.2 with a weighted mean εNd value of -18.6 ± 0.2 (MSWD 55, p 0). Finer and coarser fractions yield weighted mean values of -19.5 ± 0.3 (MSWD 6.5, p 2.2 10^{-4}) and -18.5 ± 0.2 (MSWD 78, p 0) respectively. Except for the Tsiribihina river which displays statistically different values (-18.7 ± 0.3 and -16.2 ± 0.3 for the fine and coarse fractions respectively), granulometry does not seem to notably affect εNd compositions of modern river sands, consistently with the results of Bayon et al. (2015). Granulometric differences are instead significant for the turbidite samples (Fig. 4B and Tab. 5). Note that for modern river sand samples, the uncertainty stemming from the single sampling of each river is probably much more important than the analytical uncertainty on each individual analysis.

The εNd values of the 100-250 µm fraction of 9 out of 12 the turbidite samples fall within the interval between the Mangoky (-19.1 ± 0.3) and the Tsiribihina (-16.2 ± 0.3) (Fig. 4B), the two main rivers of the study area. One core sample, at 706 ka (S17, Tab.1 and 5), presents a more negative signature (-19.3 ± 0.5), closer to that of the Onilahy (-20.5 ± 2) or the Manambolo (-20.3 ± 0.2) rivers. Two turbidite samples at 353 ka and 615 ka (S12 and S15 respectively, Tab.1 and 5) present less negative signatures (-15.4 ± 0.4 and -15.6 ± 0.3 respectively), closer to that of the Morondava river (-15.8 ± 0.3).

The transparent heavy-mineral (tHM) assemblage of the studied turbidite samples from core MOZ04-CS24 represents between 1.0% and 3.4% of the bulk sediment and mostly consists of blue-green and subordinately green-brown amphibole (46-73%tHM, ACI 9-32), with minor garnet (1-19%tHM), epidote-group minerals (2-8%tHM), zircon (1-8%tHM), tourmaline (1-6%tHM), clinopyroxene (1-9%), prismatic sillimanite (≤ 7%tHM), apatite (1-6%tHM), and rarer titanite, anatase, rutile, hypersthene, kyanite, monazite, and staurolite (ZTR 5-16). Sporadically recorded minerals include enstatite, xenotime, topaz, vesuvianite, brookite, plus a few unidentified grains.

6. Discussion

6.1. *Sediment mixing in the highly weathered soils and effects of the lateritic cover*

In tropical regions, soils are generally thick, extensively weathered and homogenized by bioturbation (e.g., termites, ants, worms) in their upper 3-4 m (Braucher et al., 2000; Breemen and Buurman, 2002; Von Blanckenburg et al., 2004). In the central plateau of SW Madagascar, lateritic soils, mostly (85 to 90 %) resulting from the chemical weathering of metamorphic gneiss or schist bedrocks can reach maximum thicknesses of 25 m (Paul et al., 2022). The typical Malagasy lateritic cover, as described by Estrade et al. (2019), is composed in its uppermost part of a pedolith (20 to 70 % of the entire lateritic profile) where soil forming processes occur and where the fabric of the parent rock is lost. It overlies a saprolite (10 to 50 % of the profile) where over 20% of the weatherable minerals of the parent bedrock are typically altered. Below, the saprock (15 to 30 % of the profile) is differentiated from the saprolite by the amount of altered weatherable minerals (< 20 %) and is closer in texture and physical strength to the bedrock that it overlies. Organic material is typically concentrated in the pedolith where bioturbation preferentially occurs, although it is seldom spread throughout it. Because bioturbation can affect the concentration of cosmogenic nuclides by mixing of deep low concentrated with shallow high concentrated grains, cosmogenic depth profiles measured in tropical areas commonly present homogenized and constant concentrations in the upper 3-4 meters and classic exponential decrease with depth below that (Braucher et al., 2000). In the case of bioturbated soils, the time required to reach steady state is expected to be longer than when bioturbation is absent (Brown et al., 1995). We quantified this time delta with equations (1) and (5) of Brown et al., (1995), for different values of denudation and bioturbation thicknesses, showing, as expected, that denudation rates mainly control the time to reach steady state (i.e., longer to reach steady state for lower denudation rates), whereas the thickness of the bioturbated interval appears less relevant (Sup. Info. 4).

The homogenized concentration throughout the bioturbated layer is generally similar to the concentration measured at the surface of a soil unaffected by bioturbation (Braucher et al., 2000; Brown et al., 1995; Von Blanckenburg et al., 2004). The impact of bioturbation thus remains limited, unless the entire soil profile is removed in a single extreme event (Von Blanckenburg et al., 2004). The long time required to alter crystalline basement into lateritic soils (typically 50 to 100 ka/m, Breemen and Buurman, 2002) and the thicknesses of these soils in Madagascar (up to 25 m, Paul et al., 2022), makes it highly unlikely that such an event could have occurred in the past 900 ka, without the ^{10}Be denudation signal reacting.

However, Brown et al. (1995) suggested that very slow denudation and deep bioturbation might impact concentrations significantly, but without providing any quantification or calculations to support this suggestion. Following equations presented in Brown et al. (1995), we investigated this issue by comparing ^{10}Be cosmogenic surface concentrations with and without bioturbation for the range of values of denudation rates and bioturbation thicknesses expected in Madagascar (figure 5). The lowest denudation rates determined in our study are 11.2 ± 2.3 mm/ka (Tsiribihina basin, Tab.3) but small basins of the central plateau affected by lateritic soils have a notably lower mean value of 7 ± 0.6 mm/ka, and rates as low as 2.4 ± 0.5 mm/ka have been measured for extremely limited basins (Brosens et al., 2023; Paul et al., 2022). Our calculation and figure 5 suggest that for true denudation rates of 7 mm/ka, bioturbation thicknesses of 440 cm would be sufficient to affect calculated denudation rates beyond the inherent uncertainties within the measurements (~15%, Table 1). Estrade et al. (2019) found pedolith thicknesses of around 3 m with the exception of one borehole reaching a pedolith thickness of 7 m. However, as explained above, only the upper part of the pedolith would be bioturbated (Braucher et al., 2000). Moreover, our results suggest that representative denudation rates for the island of Madagascar would be closer to values of 20 mm/ka (Tab. 3) or even 30 mm/ka for paleo-denudation rates (Tab. 1) than to 7 mm/ka. For such denudation rates, minimum bioturbation thicknesses of 956 cm and 1342 cm respectively (Fig. 5) would be needed to disrupt the ^{10}Be-derived denudation rates by over 15%. These thicknesses are unrealistic (Breemen and Buurman, 2002) and allow us to safely conclude that bioturbation should not be a major concern for the determination of ^{10}Be derived paleo denudation rates. Another effect of intense weathering is the development of ferricrust or ferruginous cap that may protect the landscape from erosion. Modern denudation rates measured across the island (Brosens et al., 2023, and this study) show no clear correlation with laterite thicknesses reconstructed by Paul et al. (2022). It is unclear whether a ferricrust is present and widespread in Madagascar, and although the slowest denudation rates (< 10 mm / ka) are encountered on the Central Highlands, they seem to be related to a reduced rock erodibility of the basement lithologies, rather than a higher thickness of the lateritic cover (Brosens et al., 2023).

In summary, although the presence of lateritic soils should be considered and taken into due account when measuring erosion rates in Madagascar, especially over long time periods, we are confident that their effect is limited on ^{10}Be-derived denudation rates.

6.2. *Sediment transport duration from source to sink*

Turbidites are remobilized, distal sediments. An important issue is the length of transport duration of these continental sediments from the source to the final deposition as a turbidite deposit in the deep ocean basin. A significant lag time (> 10^4-10^5 years) between the depositional ages and the denudation time would greatly affect the calculation and interpretation of our ^{10}Be concentration record. Identifying the triggering mechanisms of turbidity currents at continental margins that influence said lag time can provide information on the connectivity of the river to the submarine canyons. Three main processes trigger turbidity currents (Piper and Normark, 2009): slope failure of deltaic slopes or canyon flanks (e.g., Clare et al., 2016), hyperpycnal flows (i.e., sediment-rich, flood-type river flows triggering turbidites, Mulder and Syvitski, 1995) and dilute river plumes with low sediment concentrations (1 kg/m^3) (Parsons et al., 2001). Because none of the turbidites studied in this work present an inverse granulometric sorting, hyperpycnal flows were ruled out, although this interpretation could be challenged (e.g., Legros, 2002). Hage et al. (2019) maintained that turbidity currents can be initiated by river plumes with sediment densities as low as 0.07 kg/m^3 and in their global compilation of worldwide turbidity currents, Mulder and Syvitski (1995) show that the Morondava river has typical sediment densities of 3.7 kg/m^3. Although this sediment value may evolve through time, it is two orders of magnitude above the minimum value of Hage et al. (2019). Turbidites of the submarine Tsiribihina canyon are thus considered to be triggered either by slope failure or dilute river plumes.

Because turbidity currents can be erosive, the sediments they carry may be eroded, transported and deposited on the canyon floor several times (e.g., Ruffell et al., 2024). This is particularly true for the coarse fraction meaning that the time needed to reach a deep depocenter can be significant. In core MOZ4-CS24, turbidite events appear to be more frequent during low sea-level stands, although there is no clear correlation between sea-level and turbidite occurrence. This suggests that turbidity currents, and associated sedimentary transport occur regularly through time, although the processes involved might change depending on the sea-level (e.g., Mulder et al., 2003). As said above, an important part of the sediments transported by turbidity currents are remobilized, possibly several times, and the inherent lag time between their erosion and their deposition should be considered when measuring ^{10}Be-derived denudation rates.

Unfortunately, few studies have dated turbidites accurately enough to constrain the lag time between continental erosion and deep-sea burial, especially in tropical low denudation settings. In Monterey Bay, Stevens et al. (2014) used Optically Simulated Luminescence (OSL) to date the timing of sediment entry into the canyon head and ^{14}C ages of benthic foraminifera to constrain the depositional age of hemipelagic sediments that bound the sand horizons. They demonstrated relatively rapid, decadal-to-millennial-scale lag time between the entry of sediment into the canyon and deposition in the deep-sea fan. Nakamura et al. (1990) dated organic fractions in 1 to 3 m deep turbidites recovered from Suruga Bay, yielding radiocarbon ages between 270 ± 80 to 2270 ± 90 a BP, also suggesting rapid transport (< 2360 a) despite the lack of direct age constraints on the deposition of immediately succeeding and underlying hemipelagite deposits. These two studies where however done in regions with geological settings fundamentally different from the ones found in Madagascar. Mignard (2017) investigated the source-to-sink transport time of turbidite deposits in the Ogooué deep-sea fan on the West African equatorial margin, using radiocarbon on both vegetal debris found within the turbidites and foraminiferal assemblages separated from neighboring hemipelagic sediment layers. They found lag times between the ages found in the turbidites and associated hemipelagic layers ranging between 0.01 to 14.33 ka, with a mean of 6.33 ka.

In summary, considering the diverse uncertainties involved, a realistic lag time between the depositional ages in the fan and the ages of continental sediment erosion is in the order of a few ka. This lag time is well within the integration times associated to our calculated denudation rates (mean integration time of 21.3 ka, Tab. 1). Nevertheless, considering that the Ogooué catchment is a tectonically stable low relief region with a tropical climate, similar to Madagascar, we choose to shift our ages of 6 ka in the past in order to agree with the mean lag time measured by Mignard (2017), for a more accurate comparison of our data to climatic events of known age.

Another potential issue is the modification of the original cosmogenic signal by reworking and mixing of older sediment stored in the continental drainage basin and either depleted or enriched in cosmogenic nuclides. Because of the apparent absence of widespread terraces in the rivers considered in this work, storage and production of cosmogenic nuclides may mostly occur within the deltaic region. Accordingly, we calculated a production rate of 3.2 $at.g^{-1}.a^{-1}$ in a small basin in the lowlands, considered representative of the Mangoky delta. At this rate, assuming an average duration of sediment transport similar to that determined for the Ogooué basin (6 ka) and that all production occurs onshore with instantaneous transfer to the sea, the total production in the floodplain (Nfp) would be of of 1.9 x 10^4 $at.g^{-1}$. This represents a maximum 30 % (for sample at 614 ka) and an average 16% of measured concentrations, an error well within the bounds of the other involved uncertainties. Moreover, because Mignard et al.

(2017) dated vegetal debris, the time lag we assumed may account for both continental transport and potential storage along the continental margin. Because the drainage area considered for the Tsiribihina submarine valley (~ 140.10^3 km^2) is smaller than the area of the Ogooué catchment (~ 220.10^3 km^2) and is characterized by much higher relief and no large floodplain, a much shorter duration of onshore sediment transport than in the Ogooué catchment can be assumed. It is therefore most likely that storage on the continental margin accounted for a significant part of the considered lag time and that 1.9 10^4 at/g of cosmogenic production across the flood plain (Nfp in equation 1) represents a conservative maximum value.

To better investigate the effect of potential storage and reworking of old sediments in the drainage basin, we examined the downstream evolution of ^{10}Be concentrations for the Mangoky river which shows downstream decreasing concentrations (Sup. Info. 5), suggesting potential reworking of ^{10}Be depleted sediments temporarily stored in the catchment. This possibility is however challenged by the lack of correlation of ^{10}Be concentrations with basin area (Sup. Info. 6). If we consider sediments with initial ^{10}Be concentration as those measured by Brosens et al. (2023) in the plateau upstream ($7.5x10^5$at/g), then the thickness of reworked alluvial sediments and the time of storage required to decrease by a factor 3 the concentration measured downstream would be unrealistic, even in the case where the reworked alluvial sediments were produced during periods of higher denudation (Charreau et al., 2023, Sup. Info. 8). For instance, for a denudation of 90 mm/ka (3 times higher than the maximum value observed today), > 70% of the river sediments should come from a 50 m-thick and 500 ka-old terrace to decrease by a factor 3 the ^{10}Be concentration measured at the outlet (Sup. Info. 8). The observed downstream decrease in concentration is more likely ascribed to a change in lithology. The upper reaches of SW Madagascar rivers drain crystalline basement, whereas the lower reaches drain sandstone formations more prone to erosion, and petrographic analyses show a sharp and rapid enrichment in recycled quartz grains as the rivers leave the central plateau and cut across Mesozoic siliciclastic rocks. These observations, together with the limited extent of floodplains and fluvial terraces allows us to consider sediment reworking as a minor effect. We are therefore confident that our concentrations truly represent denudation rates and not post-erosion production.

6.3. *Source evolution*

Heavy mineral assemblages in turbidites document extensive mixing in various proportions of detritus supplied by the Tsiribihina or Manambolo rivers debouching to the north of the Tsiribihina submarine canyon, with detritus largely supplied by the Mangoky river debouching to the south. Contributions from other smaller rivers or more distant mouths (e.g., Morondava, Finerenana, Onilahy Fig. 2) are considered as minor from the heavy mineral point of view. This could be due to the limited areas of their basins, with crystalline lithologies present only in their uppermost parts. Major contribution from the Mangoky river is explained by the mainly northward littoral sand drift along the shores of SW Madagascar, as indicated by numerous deltaic spits in the region, although counter-transport locally prevails with smaller spits oriented southward in response to wave diffraction (Anthony, 2015). The Mangoky canyon, which joins the Tsiribihina submarine valley upstream of core MOZ4-CS24 site (Fig. 2), is located in an area where the continental shelf is narrower, leading to probable connection of the river to the canyon during sea level highstands.

The sediment contribution of the Mangoky versus the Tsiribihina, Manambolo and other rivers was calculated by forward mixing models (Garzanti et al., 2012) based on integrated bulk-petrography and on heavy mineral data from modern-river sands from Garzanti et al. (2022a). The results of these calculations are more accurate if end-member compositional signatures are defined by a wide set of parameters that do not display marked grain-size-dependent compositional variability and are both precisely determined and sufficiently distinct (Resentini et al., 2017). This is the case for SW Madagascar, where amphibole dominates the tHM suite of the Tsiribihina and Manambolo sands, in contrast with southern rivers where garnet is invariably abundant. Predominant contribution from the Mangoky river is thus indicated for samples characterized by higher garnet/amphibole ratio, more sillimanite, staurolite, apatite, zircon, and monazite. Sample S9 dated as 236 ka, where xenotime was detected, appears to be almost entirely derived from the Mangoky river. Samples S4, S5, S10, S15, S16a, and S20 are also mostly (75-90%) derived from the Mangoky river, whereas samples S8, S17, and S24 appear to be mainly (~60-70%) supplied by the Tsiribihina and Manambolo rivers (Tab. 6). Similarly, our ^{10}Be denudation data from the same modern-river sands, with integration times of the order of 10 ka, suggest notably larger sediment fluxes for the Mangoky (weighted mean of 3.1 ± 0.9 Mt/a) than for the Tsiribihina and Onilahy rivers which have the same weighted mean outflow (1.5 ± 0.4 Mt/a).

Garzanti et al. (2022b) found εNd signatures of -18 and -24 for the 15-500 µm fraction of sands of the Tsiribihina and Mangoky rivers, respectively, the two largest catchments of our study area. For the Tsiribihina river, our result for the finer grained fraction is comparable to that of Garzanti et al. (2022b), though the εNd values (-18.7 ± 0.3 and -16.2 ± 0.3) of the two fractions we analyzed (50-100 µm and 100-250 µm, respectively), differ significantly. In contrast, for the Mangoky river our results are much less negative, -19.1 ± 0.3 and -19.0 ± 0.3 respectively for the two size fractions, than the value of Garzanti et al. (2022b). Unlike for the Tsiribihina river, the two size fractions of the Mangoky river, agree within uncertainty, which is also true or nearly true for the other rivers we analyzed (Tab. 5). This apparent insensitivity of Nd isotopes to sediment grain size has been observed in sediments from most studied global rivers (Bayon et al., 2015). In the core samples, we found that in half of the cases for which results for two size fractions are available, the εNd values of these fractions agree within uncertainty. However, for other samples (S2, S4, S5, S17, Tab. 5), the finer fraction is about 1 to 2 εNd units less negative (Fig. 4C). As shown by Garçon et al. (2013), grain size sorting has little effect on the Nd isotope composition of river sediments. Instead, the small differences in εNd existing between the size fractions of some of the marine core samples may indicate that they were derived from sources of different average lithological composition. The slightly higher εNd of the finer fractions may imply that they originate from sources that included a greater proportion of younger and/or more mafic material than the coarser fractions. To facilitate comparison between the different samples, and considering that different minerals (such as monazite) may control the Nd budget and that most are ultra-dense and consequently strongly concentrated in the finest tail of the size distribution (Garzanti et al., 2024) (Sup. Info 6), we chose to base the rest of this discussion on the 100-250 µm fraction only.

We consider that over the past 900 ka, changes in lithologies drained by the studied rivers can be viewed as negligible. This might not be true of source regions affected by glacial processes with a high amplitude glacial-interglacial cycling, as the weathering processes operating under these two regimes might differentially impact different lithologies. However, this is unlikely to be a problem in our study area, which was never affected by glacial processes. Hence, we consider the εNd values of the studied rivers as endmembers in the provenance analysis of MOZ4-CS24 core turbidites. Figure 4B suggests that turbidite sands were sourced mainly from the Tsiribihina river, assuming that the εNd value of the 100-250 µm fraction is indeed representative of the sediments from this river. This interpretation is however in disagreement with both modern ^{10}Be and findings inferred from heavy mineral assemblages which collectively suggest that sediments were mainly sourced from the Mangoky basin (Tables 3 and 6). Siliciclastic rocks exposed close to the coast are expected to have a much less negative εNd signature than Mesoarchean to Neoproterozoic crystalline lithologies exposed on the central plateau. This is confirmed by the more radiogenic Nd isotope composition of sediments from the Morondava river, whose small basin is largely confined to the coastal plain. The εNd values MOZ4-CS24 turbidites may therefore reflect a dominant sediment contribution from the coastal region rather than a North vs. South signature. It is however unrealistic that sediments would only originate from the lower coastal areas. Although denudation rates are lower on the high central plateaus (e.g., 7.5 ± 3.0 mm/ka, Brosens et al., 2023) this vast region represents over half of the drainage area considered in this study. Should sediments be derived almost exclusively from the coastal areas, the production rate of cosmogenic nuclides would be closer to that of the Morondava basin (P_n = 3.5 at/g/a, P_{fm} = 0.04 at/g/a and P_{sm} = 0.01 at /g/a), implying rates increasing by a maximum of 26% in comparison to the rates measured with production rates calculated over the entire quartz-rich area (P_n = 4.8 at/g/a, P_{fm} = 0.04 at/g/a, P_{sm} = 0.01 at/g/a). This potential bias in the denudation rates calculated remains within uncertainties of our data. The causes of the observed discrepancy between provenance estimates inferred from Nd isotope compositions and heavy minerals remain elusive. One possibility might be a mineralogical effect, although previous studies of Nd isotopes in river sediments suggest that this is unlikely (Garçon et al., 2013). Another possibility is that the river sediment samples we analyzed are not representative of the average Nd isotope compositions of the corresponding rivers. For the Mangoky basin, the very large discrepancy between the εNd value we obtained (-19) and that of (Garzanti et al., 2022b) (-24) suggests that the Nd budget of this river's sediment load might be quite heterogeneous. Whatever the cause for this apparent contradiction, both provenance tracers show no correlation or covariation between their stratigraphic trends in the MOZ4-CS24 core and calculated denudation rates. Our data shows neither major provenance changes nor steady trends in sediments delivered to the submarine Tsiribihina canyon over the past 900 ka, and no systematic control over denudation nor relationship with glacial/interglacial cycles.

6.4. *Climate and denudation rates*

Modern denudation rates from rivers are consistent with literature values (Brosens et al., 2023; Cox et al., 2009; Wang et al., 2021) which range from 2.4 ± 0.5 mm/ka to 53 ± 13.1 mm/ka with a weighted mean average of 8.7 ± 0.4 mm/ka (MSWD 5.1, p 0), and with the higher denudation rates obtained in coastal areas, or the eastern great escarpment (weighted mean average of 20.0 ± 10.1 mm/ka), compared to the central plateau highlands (weighted mean average of 7.5 ± 3.0 mm/ka) (Brosens et al., 2023). Calculated paleo-denudation rates remained nearly constant within uncertainties over the past 900 ka, although higher than the average calculated denudation rates measured for modern-river catchments of SW Madagascar (15.7 ± 2.4 mm/ka) (Fig. 4A). This suggests that SW Madagascar has remained in near-steady state through Middle and Late Pleistocene, at least in terms of denudation.

Glacial and interglacial paleo-denudation rates from MOZ4-CS24 core turbidites yield mean weighted values of 25.7 ± 3.8 mm/ka (n = 11) and 29 ± 5 mm/ka (n = 8), respectively, thus certainly slightly higher during interglacial periods, although the two values are indistinguishable within uncertainties. Pre-hiatus (stratigraphically below) and post-hiatus (stratigraphically above) data, which likely represent syn- and post-MPT time intervals, yield weighted mean denudation rates of 28.0 ± 3.9 mm/ka (n = 7) and 24.9 ± 4.7 mm/ka (n = 12), respectively. These values are again indistinguishable within uncertainties, although syn-MPT denudation rates may have been slightly higher. During glacial periods weighted mean denudation rates are 27.1 ± 5.2 mm/ka (n = 6) and 24.0 ± 5.6 mm/ka (n = 5) for syn-MPT and post-MPT data, respectively. Weighted mean denudation rates during interglacial periods are 29.0 ± 6.0 mm/ka (n = 6) and 27.2 ± 9.1 mm/ka (n = 2) for syn-MPT and post-MPT data, respectively. Interglacial and glacial denudation are thus similar within 1 sigma before and after the MPT. This data indicates that the MPT and the Middle to Late Pleistocene glacial cycles did not significantly impact the denudation processes in SW Madagascar. However, given the characteristic times of our paleo-denudation rates (Tab. 1), the assignment to glacial or interglacial periods could be challenged.

An alternative approach to investigate the influence of climate is to compare denudation rates to the $\partial^{18}O$ values of the LR04 data from Lisiecki and Raymo (2005) averaged over the uncertainties on deposition ages and integration times associated with each denudation rate. For instance, for denudation rates of 50 mm/ka (i.e. integration time of 12ka, see Methods and Von Blanckenburg, 2005 for further explanation) measured at 150 ± 10 ka, $\partial^{18}O$ will be averaged from 140 to 172ka. Figures 6A and 6Ba show no correlation between the instantaneous (i.e., at the time of deposition of the turbidite + 6ka, Tab.1) or averaged $\partial^{18}O$ respectively compared to calculated denudation rates, respectively. To refine this test, we did simulations in which we randomly selected an age value within the uncertainty of turbidite depositional ages and averaging the $\partial^{18}O$ over the characteristic time of the denudation rate associated to the turbidite age selected. If we take the same example as above of a denudation rate of 50 mm/ka measured at 150 ± 10 ka, we randomly select an age within the uncertainty, for instance 143 ka, and integrate the ∂^{18}O values over the integration time associated to the denudation rate (12 ka, see above), so from 143 ka to 155 ka. We did 100 000 iterations for each denudation point and calculated the correlation coefficient r^2 between the so averaged ∂^{18}O and denudation rates. The best correlation coefficient obtained with this method is $r^2 = 0.1508$, indicating no relation between denudation records and ∂^{18}O data (Fig. 6). Overall, denudation rates in SW Madagascar remained steady during the past 900 ka. The lack of correlation with ∂^{18}O records of glacial/interglacial cycles indicates that climate variability has not played a major role in controlling denudation on the island.

We may however question whether the resolution of our cosmogenic data can capture the climatic signal. If the characteristic time associated with ^{10}Be derived denudation rates is too long, our record could smoothen any climate-driven variability. Following Schaller and Ehlers, (2006), we tested this potential smoothing effect by calculating an expected measured cosmogenic denudation rates if true denudation rates (i.e., the actual denudation taking place in the catchment) vary synchronously and with the same amplitude as climate variability. The modern denudation rate D_{modern} is fixed to the average value measured from modern-river sands. We then assumed that true denudation rates D_{input} covary with the ∂^{18}O data of the LR04 stack with different amplitudes relative to the D_{modern} (Fig. 7). In other words, by fixing the amplitude, we artificially force the maximal and minimal values of D_{input} that will be centered around D_{modern}. The cosmogenic integration times are calculated from the true denudation D_{input} and a mean denudation over this integration time is extracted. We test the sensitivity of ^{10}Be to variations in denudation by changing the amplitude of said variations and the D_{modern} value. The ratio given in figure 7 corresponds to the maximum of D_{input} divided by D_{modern}. This ratio is fixed by determining D_{modern} and the amplitude range of D_{input}. The resulting denudation rates that would be measured using cosmogenic ^{10}Be are given in blue in Fig.7. Results show that for denudation rates of 15 mm/ka, which is the weighted mean value of modern rivers of SW Madagascar (Tab. 3), and variations as low as 1.2 times D_{modern}, ^{10}Be accurately records variations (Fig. 7A), although these are more accurate for a ratio of 4 (Fig. 7B). The same is true for values of 10 mm/ka (Fig. 7C) and 50 mm/ka (Fig. 7D), with ratio variations of 1.5, although the resolution is better for higher D_{modern} and there is a shift of the recording for lower denudation rates. This reasoning implies that, given the range of modern denudation rates we measure, we could have captured climate-related cyclicity in denudation rates with variations as low as 1.2 times the modern values, reinforcing the conclusions that climate cyclicity has not notably influenced denudation in SW Madagascar over the past 900 ka.

Such a limited impact of climate cyclicity on denudation rates of Madagascar may be explained by the lower amplitudes of temperature and precipitation changes characterizing subtropical regions of the southern hemisphere (Chevalier et al., 2021). Although glacial periods are generally considered to be drier than interglacial periods (e.g., Litt et al., 2014; Scheff et al., 2017), this was not necessarily true for subtropical Africa (McGee, 2020). Precipitation changes associated with glacial-interglacial cycling are not well understood and poorly recorded in southern Hemisphere subtropics where long term high-resolution paleoclimatic data is lacking and even global paleoclimate models fail to correctly address, or to address at all these regions (Chevalier et al., 2017; Han et al., 2024).

In tropical regions, the monsoon is presently the main driver of the spatial and seasonal variation in precipitation and temperature, and thus the main driver of sediment production and transfer (e.g., Andermann et al., 2012; Lupker et al., 2012; Marc et al., 2019), an effect that must have been important in the past as well. For instance, variations in erosion and sediment transport to the Indus fan, driven by changing intensities of the monsoon have been documented over millennial to multimillennial timescales (Clift and Jonell, 2021).

In Madagascar, a stable-isotope study of speleothems over the past 150 ka (Voarintsoa et al., 2017) suggested that the ITCZ, which partly drives monsoons (Gadgil, 2018), shifted southwards several times through the Holocene, causing an alternation of wet and dry climates. Migrations of the ITCZ in southern tropical areas is complex and not well understood (Burns et al., 2022). Because SW Madagascar presents semi-arid settings (Fig. 1A), a southward shift of the ITCZ, and thus of the monsoon intensity, may have impacted precipitation patterns in this region, much more significantly than glacial/interglacial cyclicity. These shifts may have impacted denudation rates of the island, and similar shifts likely occurred before, although no data exists to affirm this. However, because of the short time scale (10^3 a) of such shifts (Voarintsoa et al., 2017) they are difficult to observe in cosmogenic-derived denudation rates that have an-order-of-magnitude higher integration (10^4 a).

7. Conclusion and perspectives

This cosmogenic-nuclide study sheds new light on paleo-denudation rates in the subtropics through Middle to Late Pleistocene. We find paleo denudation rates ranging from 17.4 ± 5.8 mm/ka to 73.9 ± 29.4 mm/ka. These compare well to modern denudation rates of SW Madagascar ranging from 11.2 ± 2.3 mm/ka to 30.4 ± 6.5 mm/ka. No systematic change in denudation rates were observed in SW Madagascar over the past 900 ka, in relation neither with the MPT nor glacial/interglacial cycles. Our study suggests that this interpretation does not reflect a lack of resolution, either in terms of the pace of denudation or of sample age. However, the resolution of the applied method would be insufficient to capture higher-frequency climatic changes controlled by changes in monsoon intensity associated with shifts of the ITCZ, a mechanism that has most certainly driven past climate in Madagascar. Understanding monsoonal control on denudation is limited not only by these methodological issues but even by the lack of paleoclimatic data for subtropical regions documenting the past evolution of the monsoon. Such a gap in the worldwide data is of concern and future paleoclimatic reconstructions should turn towards the tropics and the southern hemisphere to better understand planet-wide climatic systems.

As a final note we underscore that measuring denudation rates from turbidites presents a huge potential source of information especially for turbidites deposited in the vicinity of a large river, which opens the door for global compilations of paleo-denudation rates. Turbidites may include significant reworking from slope destabilization and seafloor erosion, and selecting well resolved, river connected canyons might help avoiding some of the inherent uncertainties. In any case, more quantitative data is required to better constrain the duration of storage on the continental shelf and hence the duration of submarine transport.

Acknowledgements

This study received input from detailed analysis realised in the framework of the PAMELA project led by IFREMER and TotalEnergies in collaboration with IFP Energies nouvelles, Université de Bretagne Occidentale, Université de Rennes 1, Sorbonne Université and CNRS. We thank the captain and crew of the PAMELA-MOZ4 cruise aboard R/V Pourquoi pas? and the technical staff of IFREMER for their help in data acquisition. We particularly thank Léa Faubert for the contribution on the study of the MOZ4-CS24 core during her undergraduate degree. We thank Laëtitia Leanni and Régis Braucher for the help provided during sample treatment in CEREGE. Sample analytical procedures (^{10}Be, Nd, elemental compositions) were financed by the ANR funded PANTERA project (AAPG2021, PI: Julien Charreau).

Availability Statement

All data presented in this paper is available at (Large, 2024) as an excel document. Every sheet corresponds to a table present either in the main text, or in the supplementary material of this article. This data is under a CC BY 4.0 License. If used, copied, or modified, appropriate credit must be given. The numerical dataset and processed multibeam bathymetry collected during the oceanographic cruises PAMELA-MOZ4 (Jouet and Deville, 2015, doi:10.18142/236) are stored at SISMER data repository (http://en.data.ifremer.fr/). Sediment core collected offshore Madagascar are curated at CREAM, the IFREMER core repository in Plouzané (France). Core data related to this article can be requested at:

MOZ4-CS24 http://igsn.org/bfbgx-128009 . Access to these data is however restricted and must be accepted by the partners of the PAMELA project.

References

Acosta, V.T., Schildgen, T.F., Clarke, B.A., Scherler, D., Bookhagen, B., Wittmann, H., Von Blanckenburg, F., Strecker, M.R., 2015. Effect of vegetation cover on millennial-scale landscape denudation rates in East Africa. Lithosphere 7, 408–420. https://doi.org/10.1130/L402.1

Andermann, C., Bonnet, S., Crave, A., Davy, P., Longuevergne, L., Gloaguen, R., 2012. Sediment transfer and the hydrological cycle of Himalayan rivers in Nepal. Comptes Rendus Géoscience 344, 627–635. https://doi.org/10.1016/j.crte.2012.10.009

Andò, S., Garzanti, E., 2014. Raman spectroscopy in heavy-mineral studies. Geol. Soc. Lond. Spec. Publ. 386, 395–412. https://doi.org/10.1144/SP386.2

Andò, S., Morton, A., Garzanti, E., 2014. Metamorphic grade of source rocks revealed by chemical fingerprints of detrital amphibole and garnet. Geol. Soc. Lond. Spec. Publ. 386, 351–371. https://doi.org/10.1144/SP386.5

Andriampenomanana, F., Nyblade, A.A., Wysession, M.E., Durrheim, R.J., Tilmann, F., Julià, J., Pratt, M.J., Rambolamanana, G., Aleqabi, G., Shore, P.J., Rakotondraibe, T., 2017. The structure of the crust and uppermost mantle beneath Madagascar. Geophys. J. Int. 210, 1525–1544. https://doi.org/10.1093/gji/ggx243

Anthony, E.J., 2015. Wave influence in the construction, shaping and destruction of river deltas: A review. Mar. Geol. 361, 53–78. https://doi.org/10.1016/j.margeo.2014.12.004

Antonelli, A., Smith, R.J., Perrigo, A.L., Crottini, A., Hackel, J., Testo, W., Farooq, H., Torres Jiménez, M.F., Andela, N., Andermann, T., Andriamanohera, A.M., Andriambololonera, S., Bachman, S.P., Bacon, C.D., Baker, W.J., Belluardo, F., Birkinshaw, C., Borrell, J.S., Cable, S., Canales, N.A., Carrillo, J.D., Clegg, R., Clubbe, C., Cooke, R.S.C., Damasco, G., Dhanda, S., Edler, D., Faurby, S., De Lima Ferreira, P., Fisher, B.L., Forest, F., Gardiner, L.M., Goodman, S.M., Grace, O.M., Guedes, T.B., Henniges, M.C., Hill, R., Lehmann, C.E.R., Lowry, P.P., Marline, L., Matos-Maraví, P., Moat, J., Neves, B., Nogueira, M.G.C., Onstein, R.E., Papadopulos, A.S.T., Perez-Escobar, O.A., Phelps, L.N., Phillipson, P.B., Pironon, S., Przelomska, N.A.S., Rabarimanarivo, M., Rabehevitra, D., Raharimampionona, J., Rajaonah, M.T., Rajaonary, F., Rajaovelona, L.R., Rakotoarinivo, M., Rakotoarisoa, A.A., Rakotoarisoa, S.E., Rakotomalala, H.N., Rakotonasolo, F., Ralaiveloarisoa, B.A., Ramirez-Herranz, M., Randriamamonjy, J.E.N., Randriamboavonjy, T., Randrianasolo, V., Rasolohery, A., Ratsifandrihamanana, A.N., Ravololomanana, N., Razafiniary, V., Razanajatovo, H., Razanatsoa, E., Rivers, M., Sayol, F., Silvestro, D., Vorontsova, M.S., Walker, K., Walker, B.E., Wilkin, P., Williams, J., Ziegler, T., Zizka, A., Ralimanana, H., 2022. Madagascar's extraordinary biodiversity: Evolution, distribution, and use. Science 378, eabf0869. https://doi.org/10.1126/science.abf0869

Archibald, D.B., Collins, A.S., Foden, J.D., Payne, J.L., Holden, P., Razakamanana, T., 2019. Late syn- to post-collisional magmatism in Madagascar: The genesis of the Ambalavao and Maevarano Suites. Geosci. Front. 10, 2063–2084. https://doi.org/10.1016/j.gsf.2018.07.007

Archibald, D.B., Collins, A.S., Foden, J.D., Payne, J.L., Taylor, R., Holden, P., Razakamanana, T., Clark, C., 2015. Towards unravelling the Mozambique Ocean conundrum using a triumvirate of zircon isotopic proxies on the Ambatolampy Group, central Madagascar. Tectonophysics 662, 167–182. https://doi.org/10.1016/j.tecto.2015.02.018

Archibald, D.B., Collins, A.S., Foden, J.D., Razakamanana, T., 2017. Tonian Arc Magmatism in Central Madagascar: The Petrogenesis of the Imorona-Itsindro Suite. J. Geol. 125, 271–297. https://doi.org/10.1086/691185

Bayon, G., Barrat, J.A., Etoubleau, J., Benoit, M., Bollinger, C., Révillon, S., 2009. Determination of Rare Earth Elements, Sc, Y, Zr, Ba, Hf and Th in Geological Samples by ICP-MS after Tm Addition and Alkaline Fusion. Geostand. Geoanalytical Res. 33, 51–62. https://doi.org/10.1111/j.1751-908X.2008.00880.x

Bayon, G., Toucanne, S., Skonieczny, C., André, L., Bermell, S., Cheron, S., Dennielou, B., Etoubleau, J., Freslon, N., Gauchery, T., Germain, Y., Jorry, S.J., Ménot, G., Monin, L., Ponzevera, E., Rouget, M.-L., Tachikawa, K., Barrat, J.A., 2015. Rare earth elements and neodymium isotopes in world river sediments revisited. Geochim. Cosmochim. Acta 170, 17–38. https://doi.org/10.1016/j.gca.2015.08.001

Bekaddour, T., Schlunegger, F., Vogel, H., Delunel, R., Norton, K.P., Akçar, N., Kubik, P., 2014. Paleo erosion rates and climate shifts recorded by Quaternary cut-and-fill sequences in the Pisco valley, central Peru. Earth Planet. Sci. Lett. 390, 103–115. https://doi.org/10.1016/j.epsl.2013.12.048

Berends, C.J., Köhler, P., Lourens, L.J., Wal, R.S.W., 2021. On the Cause of the Mid-Pleistocene Transition. Rev. Geophys. 59. https://doi.org/10.1029/2020RG000727

Berner, R.A., Lasaga, A.C., Garrels, R.M., 1983. The carbonate-silicate geochemical cycle and its effect on atmospheric carbon dioxide over the past 100 million years. Am. J. Sci. 283, 641–683. https://doi.org/10.2475/ajs.283.7.641

Besairie, H., 1972. Géologie de Madagascar. I. Les terrains sédimentaires.

Boger, S.D., Maas, R., Pastuhov, M., Macey, P.H., Hirdes, W., Schulte, B., Fanning, C.M., Ferreira, C.A.M., Jenett, T., Dallwig, R., 2019. The tectonic domains of southern and western Madagascar. Precambrian Res. 327, 144–175. https://doi.org/10.1016/j.precamres.2019.03.005

Bouvier, A., Vervoort, J.D., Patchett, P.J., 2008. The Lu–Hf and Sm–Nd isotopic composition of CHUR: Constraints from unequilibrated chondrites and implications for the bulk composition of terrestrial planets. Earth Planet. Sci. Lett. 273, 48–57. https://doi.org/10.1016/j.epsl.2008.06.010

Braucher, R., Bourlès, D.L., Brown, E.T., Colin, F., Muller, J.-P., Braun, J.-J., Delaune, M., Edou Minko, A., Lescouet, C., Raisbeck, G.M., Yiou, F., 2000. Application of in situ-produced cosmogenic 10Be and 26Al to the study of lateritic soil development in tropical forest: theory and examples from Cameroon and Gabon. Chem. Geol. 170, 95–111. https://doi.org/10.1016/S0009-2541(99)00243-0

Braucher, R., Guillou, V., Bourlès, D.L., Arnold, M., Aumaître, G., Keddadouche, K., Nottoli, E., 2015. Preparation of ASTER in-house 10Be/9Be standard solutions. Nucl. Instrum. Methods Phys. Res. Sect. B Beam Interact. Mater. At. 361, 335–340. https://doi.org/10.1016/j.nimb.2015.06.012

Braucher, R., Merchel, S., Borgomano, J., Bourlès, D.L., 2011. Production of cosmogenic radionuclides at great depth: A multi element approach. Earth Planet. Sci. Lett. 309, 1–9. https://doi.org/10.1016/j.epsl.2011.06.036

Breemen, N. van, Buurman, P., 2002. Soil formation, 2nd ed. ed. Kluwer Academic Publishers, Dordrecht.

Brosens, L., Broothaerts, N., Campforts, B., Jacobs, L., Razanamahandry, V.F., Van Moerbeke, Q., Bouillon, S., Razafimbelo, T., Rafolisy, T., Govers, G., 2022. Under pressure: Rapid lavaka erosion and floodplain sedimentation in central Madagascar. Sci. Total Environ. 806, 150483. https://doi.org/10.1016/j.scitotenv.2021.150483

Brosens, L., Cox, R., Campforts, B., Jacobs, L., Vanacker, V., Bierman, P., Razanamahandry, V.F., Rakotondrazafy, A.F.M., Razafimbelo, T., Rafolisy, T., Govers, G., 2023. The slow downwearing of Madagascar: Inferring patterns and controls on long-term basin-averaged erosion rates from *in situ* ^{10}Be at the catchment and regional level. Earth Surf. Process. Landf. esp.5586. https://doi.org/10.1002/esp.5586

Brown, E.T., Edmond, J.M., Raisbeck, G.M., Yiou, F., Kurz, M.D., Brook, E.J., 1991. Examination of surface exposure ages of Antarctic moraines using in situ produced 10Be and 26Al. Geochim. Cosmochim. Acta 55, 2269–2283. https://doi.org/10.1016/0016-7037(91)90103-C

Brown, E.T., Stallard, R.F., Larsen, M.C., Raisbeck, G.M., Yiou, F., 1995. Denudation rates determined from the accumulation of in situ-produced 10Be in the luquillo experimental forest, Puerto Rico. Earth Planet. Sci. Lett. 129, 193–202. https://doi.org/10.1016/0012-821X(94)00249-X

Burns, S.J., McGee, D., Scroxton, N., Kinsley, C.W., Godfrey, L.R., Faina, P., Ranivoharimanana, L., 2022. Southern Hemisphere controls on ITCZ variability in southwest Madagascar over the past 117,000 years. Quat. Sci. Rev. 276, 107317. https://doi.org/10.1016/j.quascirev.2021.107317

Charreau, J., Blard, P., Zumaque, J., Martin, L.C.P., Delobel, T., Szafran, L., 2019. Basinga: A cell-by-cell GIS toolbox for computing basin average scaling factors, cosmogenic production rates and denudation rates. Earth Surf. Process. Landf. 44, 2349–2365. https://doi.org/10.1002/esp.4649

Charreau, J., Blard, P.-H., Lavé, J., Dominguez, S., Li, W.S., 2023. Unsteady topography in the eastern Tianshan due to imbalance between denudation and crustal thickening. Tectonophysics 848, 229702. https://doi.org/10.1016/j.tecto.2022.229702

Charreau, J., Blard, P.-H., Puchol, N., Avouac, J.-P., Lallier-Vergès, E., Bourlès, D., Braucher, R., Gallaud, A., Finkel, R., Jolivet, M., Chen, Y., Roy, P., 2011. Paleo-erosion rates in Central Asia since 9Ma: A transient increase at the onset of Quaternary glaciations? Earth Planet. Sci. Lett. 304, 85–92. https://doi.org/10.1016/j.epsl.2011.01.018

Charreau, J., Lavé, J., France-Lanord, C., Puchol, N., Blard, P., Pik, R., Gajurel, A.P., ASTER Team, 2021. A 6 Ma record of palaeodenudation in the central Himalayas from in situ cosmogenic ^{10}Be in the Surai section. Basin Res. 33, 1218–1239. https://doi.org/10.1111/bre.12511

Chevalier, M., Brewer, S., Chase, B.M., 2017. Qualitative assessment of PMIP3 rainfall simulations across the eastern African monsoon domains during the mid-Holocene and the Last Glacial Maximum. Quat. Sci. Rev. 156, 107–120. https://doi.org/10.1016/j.quascirev.2016.11.028

Chevalier, M., Chase, B.M., Quick, L.J., Dupont, L.M., Johnson, T.C., 2021. Temperature change in subtropical southeastern Africa during the past 790,000 yr. Geology 49, 71–75. https://doi.org/10.1130/G47841.1

Clare, M.A., Hughes Clarke, J.E., Talling, P.J., Cartigny, M.J.B., Pratomo, D.G., 2016. Preconditioning and triggering of offshore slope failures and turbidity currents revealed by most detailed monitoring yet at a fjord-head delta. Earth Planet. Sci. Lett. 450, 208–220. https://doi.org/10.1016/j.epsl.2016.06.021

Clift, P.D., 2006. Controls on the erosion of Cenozoic Asia and the flux of clastic sediment to the ocean. Earth Planet. Sci. Lett. 241, 571–580. https://doi.org/10.1016/j.epsl.2005.11.028

Clift, P.D., Jonell, T.N., 2021. Monsoon controls on sediment generation and transport: Mass budget and provenance constraints from the Indus River catchment, delta and submarine fan over tectonic and multimillennial timescales. Earth-Sci. Rev. 220, 103682. https://doi.org/10.1016/j.earscirev.2021.103682

Codilean, A.T., 2006. Calculation of the cosmogenic nuclide production topographic shielding scaling factor for large areas using DEMs. Earth Surf. Process. Landf. 31, 785–794. https://doi.org/10.1002/esp.1336

Cox, R., Armstrong, R.A., Ashwal, L.D., 1998. Sedimentology, geochronology and provenance of the Proterozoic Itremo Group, central Madagascar, and implications for pre-Gondwana palaeogeography. J. Geol. Soc. 155, 1009–1024. https://doi.org/10.1144/gsjgs.155.6.1009

Cox, R., Bierman, P., Jungers, M.C., Rakotondrazafy, A.F.M., 2009. Erosion Rates and Sediment Sources in Madagascar Inferred from ^{10}Be Analysis of Lavaka, Slope, and River Sediment. J. Geol. 117, 363–376. https://doi.org/10.1086/598945

Delaunay, A., 2018. Les mouvements verticaux de Madagascar (90 - 0 Ma) : une analyse couplée des formes du relief et de l’enregistrement sédimentaire des marges ouest malgaches. Rennes 1.

Dunai, T.J., 2000. Scaling factors for production rates of in situ produced cosmogenic nuclides: a critical reevaluation. Earth Planet. Sci. Lett. 176, 157–169. https://doi.org/10.1016/S0012-821X(99)00310-6

Estrade, G., Marquis, E., Smith, M., Goodenough, K., Nason, P., 2019. REE concentration processes in ion adsorption deposits: Evidence from the Ambohimirahavavy alkaline complex in Madagascar. Ore Geol. Rev. 112, 103027. https://doi.org/10.1016/j.oregeorev.2019.103027

Fisher, G.B., Luna, L. V., Amidon, W.H., Burbank, D.W., de Boer, B., Stap, L.B., Bookhagen, B., Godard, V., Oskin, M.E., Alonso, R.N., Tuenter, E., Lourens, L.J., 2023. Milankovitch-paced erosion in the southern Central Andes. Nat. Commun. 14. https://doi.org/10.1038/s41467-023-36022-0

Fuller, T.K., Perg, L.A., Willenbring, J.K., Lepper, K., 2009. Field evidence for climate-driven changes in sediment supply leading to strath terrace formation. Geology 37, 467–470. https://doi.org/10.1130/G25487A.1

Gadgil, S., 2018. The monsoon system: Land–sea breeze or the ITCZ? J. Earth Syst. Sci. 127, 1. https://doi.org/10.1007/s12040-017-0916-x

Galy, V., France-Lanord, C., Beyssac, O., Faure, P., Kudrass, H., Palhol, F., 2007. Efficient organic carbon burial in the Bengal fan sustained by the Himalayan erosional system. Nature 450, 407–410. https://doi.org/10.1038/nature06273

Garcin, Y., Schildgen, T.F., Torres Acosta, V., Melnick, D., Guillemoteau, J., Willenbring, J., Strecker, M.R., 2017. Short-lived increase in erosion during the African Humid Period: Evidence from the northern Kenya Rift. Earth Planet. Sci. Lett. 459, 58–69. https://doi.org/10.1016/j.epsl.2016.11.017

Garçon, M., Chauvel, C., France-Lanord, C., Huyghe, P., Lavé, J., 2013. Continental sedimentary processes decouple Nd and Hf isotopes. Geochim. Cosmochim. Acta 121, 177–195. https://doi.org/10.1016/j.gca.2013.07.027

Garzanti, E., 2017. The Maturity Myth In Sedimentology and Provenance Analysis. J. Sediment. Res. 87, 353–365. https://doi.org/10.2110/jsr.2017.17

Garzanti, E., Andò, S., 2019. Heavy Minerals for Junior Woodchucks. Minerals 9, 148. https://doi.org/10.3390/min9030148

Garzanti, E., Andò, S., 2007. Chapter 20 Heavy Mineral Concentration in Modern Sands: Implications for Provenance Interpretation, in: Developments in Sedimentology. Elsevier, pp. 517–545. https://doi.org/10.1016/S0070-4571(07)58020-9

Garzanti, E., Bayon, G., Barbarano, M., Resentini, A., Vezzoli, G., Pastore, G., Levacher, M., Adeaga, O., 2024. Anatomy of Niger and Benue river sediments from clay to granule: grain-size dependence and provenance budgets. J. Sediment. Res. https://doi.org/10.2110/jsr.2024.024

Garzanti, E., Bayon, G., Dinis, P., Vermeesch, P., Pastore, G., Resentini, A., Barbarano, M., Ncube, L., Van Niekerk, H.J., 2022a. The Segmented Zambezi Sedimentary System from Source to Sink: 2. Geochemistry, Clay Minerals, and Detrital Geochronology. J. Geol. 130, 171–208. https://doi.org/10.1086/719166

Garzanti, E., Bayon, G., Vermeesch, P., Barbarano, M., Pastore, G., Resentini, A., Dennielou, B., Jouet, G., 2022b. The Zambezi deep-sea fan: mineralogical, REE, Zr/Hf, Nd-isotope, and zircon-age variability in feldspar-rich passive-margin turbidites. J. Sediment. Res. 92, 1022–1043. https://doi.org/10.2110/jsr.2022.033

Garzanti, E., Resentini, A., Vezzoli, G., Andò, S., Malusà, M., Padoan, M., 2012. Forward compositional modelling of Alpine orogenic sediments. Sediment. Geol. 280, 149–164. https://doi.org/10.1016/j.sedgeo.2012.03.012

Godard, V., Bourles, D.L., Spinabella, F., Burbank, D.W., Bookhagen, B., Fisher, G.B., Moulin, A., Leanni, L., 2014. Dominance of tectonics over climate in Himalayan denudation. Geology 42, 243–246. https://doi.org/10.1130/G35342.1

Gonzalez, V.S., Bierman, P.R., Nichols, K.K., Rood, D.H., 2016. Long-term erosion rates of Panamanian drainage basins determined using in situ 10 Be. Geomorphology 275, 1–15. https://doi.org/10.1016/j.geomorph.2016.04.025

Granger, D.E., Kirchner, J.W., Finkel, R., 1996. Spatially Averaged Long-Term Erosion Rates Measured from in Situ-Produced Cosmogenic Nuclides in Alluvial Sediment. J. Geol. 104, 249–257. https://doi.org/10.1086/629823

Grischott, R., Kober, F., Lupker, M., Reitner, J.M., Drescher-Schneider, R., Hajdas, I., Christl, M., Willett, S.D., 2017. Millennial scale variability of denudation rates for the last 15 kyr inferred from the detrital ^{10}Be record of Lake Stappitz in the Hohe Tauern massif, Austrian Alps. The Holocene 27, 1914–1927. https://doi.org/10.1177/0959683617708451

Haeuselmann, P., Granger, D.E., Jeannin, P.-Y., Lauritzen, S.-E., 2007. Abrupt glacial valley incision at 0.8 Ma dated from cave deposits in Switzerland. Geology 35, 143. https://doi.org/10.1130/G23094A

Hage, S., Cartigny, M.J.B., Sumner, E.J., Clare, M.A., Hughes Clarke, J.E., Talling, P.J., Lintern, D.G., Simmons, S.M., Silva Jacinto, R., Vellinga, A.J., Allin, J.R., Azpiroz-Zabala, M., Gales, J.A., Hizzett, J.L., Hunt, J.E., Mozzato, A., Parsons, D.R., Pope, E.L., Stacey, C.D., Symons, W.O., Vardy, M.E., Watts, C., 2019. Direct Monitoring Reveals Initiation of Turbidity Currents From Extremely Dilute River Plumes. Geophys. Res. Lett. 46, 11310–11320. https://doi.org/10.1029/2019GL084526

Hallet, B., 1996. Glacial quarrying: a simple theoretical model. Ann. Glaciol. 22, 1–8. https://doi.org/10.3189/1996AoG22-1-1-8

Han, Z., Power, K., Li, G., Zhang, Q., 2024. Impacts of Mid-Pliocene Ice Sheets and Vegetation on Afro-Asian Summer Monsoon Rainfall Revealed by EC-Earth Simulations. Geophys. Res. Lett. 51, e2023GL106145. https://doi.org/10.1029/2023GL106145

Hay, W.W., Sloan, J.L., Wold, C.N., 1988. Mass/age distribution and composition of sediments on the ocean floor and the global rate of sediment subduction. J. Geophys. Res. Solid Earth 93, 14933–14940. https://doi.org/10.1029/JB093iB12p14933

Herman, F., Seward, D., Valla, P.G., Carter, A., Kohn, B., Willett, S.D., Ehlers, T.A., 2013. Worldwide acceleration of mountain erosion under a cooling climate. Nature 504, 423–426. https://doi.org/10.1038/nature12877

Hidy, A.J., Gosse, J.C., Blum, M.D., Gibling, M.R., 2014. Glacial–interglacial variation in denudation rates from interior Texas, USA, established with cosmogenic nuclides. Earth Planet. Sci. Lett. 390, 209–221. https://doi.org/10.1016/j.epsl.2014.01.011

Hu, Y., Li, D., Liu, J., 2007. Abrupt seasonal variation of the ITCZ and the Hadley circulation. Geophys. Res. Lett. 34, L18814. https://doi.org/10.1029/2007GL030950

Hubert, J.F., 1962. A Zircon-Tourmaline-Rutile Maturity Index and the Interdependence of the Composition of Heavy Mineral Assemblages with the Gross Composition and Texture of Sandstones. SEPM J. Sediment. Res. Vol. 32. https://doi.org/10.1306/74D70CE5-2B21-11D7-8648000102C1865D

Jouet, G., Deville, E., 2015. PAMELA-MOZ04 cruise,Pourquoi pas ? R/V.

https://doi.org/10.17600/15000700

Kohl, C.P., Nishiizumi, K., 1992. Chemical isolation of quartz for measurement of in-situ -produced cosmogenic nuclides. Geochim. Cosmochim. Acta 56, 3583–3587. https://doi.org/10.1016/0016-7037(92)90401-4

Koppes, M., Hallet, B., 2006. Erosion rates during rapid deglaciation in Icy Bay, Alaska. J. Geophys. Res. 111, F02023. https://doi.org/10.1029/2005JF000349

Korschinek, G., Bergmaier, A., Faestermann, T., Gerstmann, U.C., Knie, K., Rugel, G., Wallner, A., Dillmann, I., Dollinger, G., Von Gostomski, Ch.L., Kossert, K., Maiti, M., Poutivtsev, M., Remmert, A., 2010. A new value for the half-life of 10Be by Heavy-Ion Elastic Recoil Detection and liquid scintillation counting. Nucl. Instrum. Methods Phys. Res. Sect. B Beam Interact. Mater. At. 268, 187–191. https://doi.org/10.1016/j.nimb.2009.09.020

Kuhlemann, J., Frisch, W., Székely, B., Dunkl, I., Kàzmer, M., 2002. Post-collisional sediment budget history of the Alps: tectonic versus climatic control. Int. J. Earth Sci. 91, 818–837. https://doi.org/10.1007/s00531-002-0266-y

Large, E., 2024. Large et al. Near steady denudation rates during the late Pleistocene in the tropics. https://doi.org/10.17632/VD3X5TV4HW.1

Legros, F., 2002. Can Dispersive Pressure Cause Inverse Grading in Grain Flows? J. Sediment. Res. 72, 166–170. https://doi.org/10.1306/041301720166

Lenard, S.J.P., Lavé, J., France-Lanord, C., Aumaître, G., Bourlès, D.L., Keddadouche, K., 2020. Steady erosion rates in the Himalayas through late Cenozoic climatic changes. Nat. Geosci. 13, 448–452. https://doi.org/10.1038/s41561-020-0585-2

Lisiecki, L.E., Raymo, M.E., 2005. A Pliocene-Pleistocene stack of 57 globally distributed benthic $\delta^{18}O$ records. Paleoceanography 20, 2004PA001071. https://doi.org/10.1029/2004PA001071

Litt, T., Pickarski, N., Heumann, G., Stockhecke, M., Tzedakis, P.C., 2014. A 600,000 year long continental pollen record from Lake Van, eastern Anatolia (Turkey). Quat. Sci. Rev. 104, 30–41. https://doi.org/10.1016/j.quascirev.2014.03.017

Lupker, M., Blard, P.-H., Lavé, J., France-Lanord, C., Leanni, L., Puchol, N., Charreau, J., Bourlès, D., 2012. 10Be-derived Himalayan denudation rates and sediment budgets in the Ganga basin. Earth Planet. Sci. Lett. 333–334, 146–156. https://doi.org/10.1016/j.epsl.2012.04.020

Madella, A., Delunel, R., Akçar, N., Schlunegger, F., Christl, M., 2018. 10Be-inferred paleo-denudation rates imply that the mid-Miocene western central Andes eroded as slowly as today. Sci. Rep. 8, 2299. https://doi.org/10.1038/s41598-018-20681-x

Marc, O., Behling, R., Andermann, C., Turowski, J.M., Illien, L., Roessner, S., Hovius, N., 2019. Long-term erosion of the Nepal Himalayas by bedrock landsliding: the role of monsoons, earthquakes and giant landslides. Earth Surf. Dyn. 7, 107–128. https://doi.org/10.5194/esurf-7-107-2019

Mariotti, A., Blard, P.-H., Charreau, J., Petit, C., Molliex, S., the ASTER Team, 2019.

Denudation systematics inferred from in situ cosmogenic ¹⁰Be concentrations in fine (50–100 µm) and medium (100–250 µm) sediments of the Var River basin, southern French Alps. Earth Surf. Dyn. 7, 1059–1074. https://doi.org/10.5194/esurf-7-1059-2019

Mariotti, A., Blard, P.-H., Charreau, J., Toucanne, S., Jorry, S.J., Molliex, S., Bourlès, D.L., Aumaître, G., Keddadouche, K., 2021. Nonlinear forcing of climate on mountain denudation during glaciations. Nat. Geosci. 14, 16–22. https://doi.org/10.1038/s41561-020-00672-2

Marshall, J.A., Roering, J.J., Gavin, D.G., Granger, D.E., 2017. Late Quaternary climatic controls on erosion rates and geomorphic processes in western Oregon, USA. Geol. Soc. Am. Bull. 129, 715–731. https://doi.org/10.1130/B31509.1

Maslin, M.A., Haug, G.H., Sarnthein, M., Tiedemann, R., 1996. The progressive intensification of northern hemisphere glaciation as seen from the North Pacific. Geol. Rundsch. 85, 452–465. https://doi.org/10.1007/BF02369002

McGee, D., 2020. Glacial–Interglacial Precipitation Changes. Annu. Rev. Mar. Sci. 12, 525–557. https://doi.org/10.1146/annurev-marine-010419-010859

Melluso, L., Tucker, R.D., Cucciniello, C., Le Roex, A.P., Morra, V., Zanetti, A., Rakotoson, R.L., 2018. The magmatic evolution and genesis of the Quaternary basanite-trachyphonolite suite of Itasy (Madagascar) as inferred by geochemistry, Sr-Nd-Pb isotopes and trace element distribution in coexisting phases. Lithos 310–311, 50–64. https://doi.org/10.1016/j.lithos.2018.04.003

Métivier, F., 2002. On the use of sedimentation rates in deciphering global change. Geophys. Res. Lett. 29. https://doi.org/10.1029/2002GL015261

Mignard, S., 2017. Transport et accumulation de matière organique dans le système turbiditique de l'Ogooué (Gabon). Université de Bordeaux.

Molnar, P., 2004. LATE CENOZOIC INCREASE IN ACCUMULATION RATES OF TERRESTRIAL SEDIMENT: How Might Climate Change Have Affected Erosion Rates? Annu. Rev. Earth Planet. Sci. 32, 67–89. https://doi.org/10.1146/annurev.earth.32.091003.143456

Molnar, P., England, P., 1990. Late Cenozoic uplift of mountain ranges and global climate change: chicken or egg? Nature 346, 29–34. https://doi.org/10.1038/346029a0

Moon, S., Page Chamberlain, C., Blisniuk, K., Levine, N., Rood, D.H., Hilley, G.E., 2011. Climatic control of denudation in the deglaciated landscape of the Washington Cascades. Nat. Geosci. 4, 469–473. https://doi.org/10.1038/ngeo1159

Mulder, T., Syvitski, J.P.M., 1995. Turbidity Currents Generated at River Mouths during Exceptional Discharges to the World Oceans. J. Geol. 103, 285–299. https://doi.org/10.1086/629747

Mulder, T., Syvitski, J.P.M., Migeon, S., Faugères, J.-C., Savoye, B., 2003. Marine hyperpycnal flows: initiation, behavior and related deposits. A review. Mar. Pet. Geol. 20, 861–882. https://doi.org/10.1016/j.marpetgeo.2003.01.003

Nakamura, T., Shiki, T., Nakai, N., 1990. Variations in 14C ages of various organic fractions in a turbidite sediment core from Suruga Trough. Geochem. J. 24, 47–56. https://doi.org/10.2343/geochemj.24.47

Olen, S.M., Bookhagen, B., Strecker, M.R., 2016. Role of climate and vegetation density in modulating denudation rates in the Himalaya. Earth Planet. Sci. Lett. 445, 57–67. https://doi.org/10.1016/j.epsl.2016.03.047

Paquette, J.-L., Moine, B., Rakotondrazafy, M.A.F., 2003. ID-TIMS using the step-wise dissolution technique versus ion microprobe U–Pb dating of metamict Archean zircons from NE Madagascar. Precambrian Res. 121, 73–84. https://doi.org/10.1016/S0301-9268(02)00200-0

Parsons, J.D., Bush, J.W.M., Syvitski, J.P.M., 2001. Hyperpycnal plume formation from riverine outflows with small sediment concentrations. Sedimentology 48, 465–478. https://doi.org/10.1046/j.1365-3091.2001.00384.x

Paul, J.D., Eakin, C.M., 2017. Mantle upwelling beneath Madagascar: evidence from receiver function analysis and shear wave splitting. J. Seismol. 21, 825–836. https://doi.org/10.1007/s10950-016-9637-x

Paul, J.D., Radimilahy, A., Randrianalijaona, R., Mulyakova, T., 2022. Lateritic processes in Madagascar and the link with agricultural and socioeconomic conditions. J. Afr. Earth Sci. 196, 104681. https://doi.org/10.1016/j.jafrearsci.2022.104681

Piper, D.J.W., Normark, W.R., 2009. Processes That Initiate Turbidity Currents and Their Influence on Turbidites: A Marine Geology Perspective. J. Sediment. Res. 79, 347–362. https://doi.org/10.2110/jsr.2009.046

Portenga, E.W., Bierman, P.R., 2011. Understanding Earth's eroding surface with 10Be. GSA Today 21, 4–10. https://doi.org/10.1130/G111A.1

Pratt, M.J., Wysession, M.E., Aleqabi, G., Wiens, D.A., Nyblade, A.A., Shore, P., Rambolamanana, G., Andriampenomanana, F., Rakotondraibe, T., Tucker, R.D., Barruol, G., Rindraharisaona, E., 2017. Shear velocity structure of the crust and upper mantle of Madagascar derived from surface wave tomography. Earth Planet. Sci. Lett. 458, 405–417. https://doi.org/10.1016/j.epsl.2016.10.041

Puchol, N., Charreau, J., Blard, P.-H., Lavé, J., Dominguez, S., Pik, R., Saint-Carlier, D., ASTER Team, 2017. Limited impact of Quaternary glaciations on denudation rates in Central Asia. Geol. Soc. Am. Bull. 129, 479–499. https://doi.org/10.1130/B31475.1

Resentini, A., Goren, L., Castelltort, S., Garzanti, E., 2017. Partitioning sediment flux by provenance and tracing erosion patterns in Taiwan. J. Geophys. Res. Earth Surf. 122, 1430–1454. https://doi.org/10.1002/2016JF004026

Roberts, G.G., Paul, J.D., White, N., Winterbourne, J., 2012. Temporal and spatial evolution of dynamic support from river profiles: A framework for Madagascar: DYNAMIC SUPPORT OF MADAGASCAR. Geochem. Geophys. Geosystems 13, n/a-n/a. https://doi.org/10.1029/2012GC004040

Roig, J., Tucker, R., Delor, C., Peters, S., Théveniaut, H., 2012. Carte Géologique de la

République de Madagascar à 1/1,000,000. Ministère Mines PGRM Antananarivo Répub. Madag. 1.

Rosenblum, S., 1958. Magnetic susceptibilities of minerals in the Frantz Isodynamic magnetic separator1. Am. Mineral. 43, 170–173.

Rufer, D., Preusser, F., Schreurs, G., Gnos, E., Berger, A., 2014. Late Quaternary history of the Vakinankaratra volcanic field (central Madagascar): insights from luminescence dating of phreatomagmatic eruption deposits. Bull. Volcanol. 76, 817. https://doi.org/10.1007/s00445-014-0817-7

Ruffell, S.C., Talling, P.J., Baker, M.L., Pope, E.L., Heijnen, M.S., Jacinto, R.S., Cartigny, M.J.B., Simmons, S.M., Clare, M.A., Heerema, C.J., McGhee, C., Hage, S., Hasenhündl, M., Parsons, D.R., 2024. Time-lapse surveys reveal patterns and processes of erosion by exceptionally powerful turbidity currents that flush submarine canyons: A case study of the Congo Canyon. Geomorphology 463, 109350. https://doi.org/10.1016/j.geomorph.2024.109350

Sadler, P.M., 1981. Sediment Accumulation Rates and the Completeness of Stratigraphic Sections. J. Geol. 89, 569–584. https://doi.org/10.1086/628623

Schaller, M., Ehlers, T.A., 2006. Limits to quantifying climate driven changes in denudation rates with cosmogenic radionuclides. Earth Planet. Sci. Lett. 248, 153–167. https://doi.org/10.1016/j.epsl.2006.05.027

Schaller, M., von Blanckenburg, F., Veldkamp, A., Tebbens, L.A., Hovius, N., Kubik, P.W., 2002. A 30 000 yr record of erosion rates from cosmogenic 10Be in Middle European river terraces. Earth Planet. Sci. Lett. 204, 307–320.

Scheff, J., Seager, R., Liu, H., Coats, S., 2017. Are Glacials Dry? Consequences for Paleoclimatology and for Greenhouse Warming. J. Clim. 30, 6593–6609. https://doi.org/10.1175/JCLI-D-16-0854.1

Schildgen, T.F., Van Der Beek, P.A., Sinclair, H.D., Thiede, R.C., 2018. Spatial correlation bias in late-Cenozoic erosion histories derived from thermochronology. Nature 559, 89–93. https://doi.org/10.1038/s41586-018-0260-6

Stephenson, S.N., White, N.J., Li, T., Robinson, L.F., 2019. Disentangling interglacial sea level and global dynamic topography: Analysis of Madagascar. Earth Planet. Sci. Lett. 519, 61–69. https://doi.org/10.1016/j.epsl.2019.04.029

Stevens, T., Paull, C.K., Ussler, W., McGann, M., Buylaert, J.-P., Lundsten, E., 2014. The timing of sediment transport down Monterey Submarine Canyon, offshore California. Geol. Soc. Am. Bull. 126, 103–121. https://doi.org/10.1130/B30931.1

Thomas, R.J., De Waele, B., Schofield, D.I., Goodenough, K.M., Horstwood, M., Tucker, R., Bauer, W., Annells, R., Howard, K., Walsh, G., Rabarimanana, M., Rafahatelo, J.M., Ralison, A.V., Randriamananjara, T., 2009. Geological evolution of the Neoproterozoic Bemarivo Belt, northern Madagascar. Precambrian Res. 172, 279–300. https://doi.org/10.1016/j.precamres.2009.04.008

Tucker, R.D., Roig, J.Y., Macey, P.H., Delor, C., Amelin, Y., Armstrong, R.A., Rabarimanana, M.H., Ralison, A.V., 2011. A new geological framework for south-central Madagascar, and its relevance to the “out-of-Africa” hypothesis. Precambrian Res. 185, 109–130. https://doi.org/10.1016/j.precamres.2010.12.008

Tucker, R.D., Roig, J.Y., Moine, B., Delor, C., Peters, S.G., 2014. A geological synthesis of the Precambrian shield in Madagascar. J. Afr. Earth Sci. 94, 9–30. https://doi.org/10.1016/j.jafrearsci.2014.02.001

Vermeesch, P., 2018. IsoplotR: A free and open toolbox for geochronology. Geosci. Front. 9, 1479–1493. https://doi.org/10.1016/j.gsf.2018.04.001

Voarintsoa, N.R.G., Railsback, L.B., Brook, G.A., Wang, L., Kathayat, G., Cheng, H., Li, X., Edwards, R.L., Rakotondrazafy, A.F.M., Madison Razanatseheno, M.O., 2017. Three distinct Holocene intervals of stalagmite deposition and nondeposition revealed in NW Madagascar, and their paleoclimate implications. Clim. Past 13, 1771–1790. https://doi.org/10.5194/cp-13-1771-2017

Von Blanckenburg, F., 2005. The control mechanisms of erosion and weathering at basin scale from cosmogenic nuclides in river sediment. Earth Planet. Sci. Lett. 237, 462–479. https://doi.org/10.1016/j.epsl.2005.06.030

Von Blanckenburg, F., Bouchez, J., 2014. River fluxes to the sea from the ocean’s 10Be/9Be ratio. Earth Planet. Sci. Lett. 387, 34–43. http://dx.doi.org/10.1016/j.epsl.2013.11.004

Von Blanckenburg, F., Hewawasam, T., Kubik, P.W., 2004. Cosmogenic nuclide evidence for low weathering and denudation in the wet, tropical highlands of Sri Lanka. J. Geophys. Res. Earth Surf. 109, 2003JF000049. https://doi.org/10.1029/2003JF000049

Wang, Y., Willett, S.D., Wu, D., Haghipour, N., Christl, M., 2021. Retreat of the Great Escarpment of Madagascar From Geomorphic Analysis and Cosmogenic. Geochem. Geophys. Geosystems 25 p. https://doi.org/10.3929/ETHZ-B-000519815

West, A.J., 2012. Thickness of the chemical weathering zone and implications for erosional and climatic drivers of weathering and for carbon-cycle feedbacks. Geology 40, 811–814. https://doi.org/10.1130/G33041.1

Willenbring, J.K., von Blanckenburg, F., 2010. Long-term stability of global erosion rates and weathering during late-Cenozoic cooling. Nature 465, 211–214. https://doi.org/10.1038/nature09044

Zachos, J., Pagani, M., Sloan, L., Thomas, E., Billups, K., 2001. Trends, Rhythms, and Aberrations in Global Climate 65 Ma to Present. Science 292, 686–693. https://doi.org/10.1126/science.1059412

Zhang, P., Molnar, P., Downs, W.R., 2001. Increased sedimentation rates and grain sizes 2–4 Myr ago due to the influence of climate change on erosion rates. Nature 410, 891–897. https://doi.org/10.1038/35073504

Figures

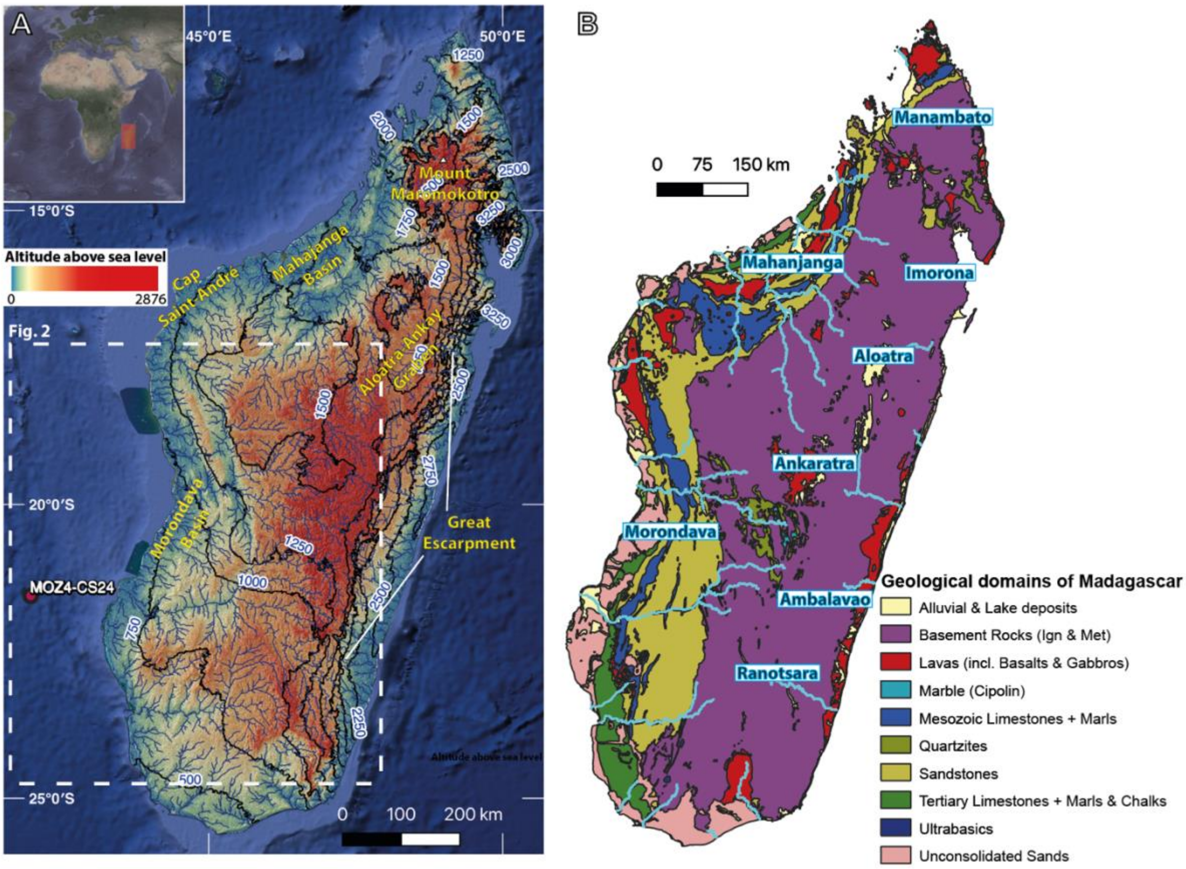

Figure 1 : Location, topography and geology of the island of Madagascar. A/ Black continuous lines are the isohyetals for 250 mm/a rainfall from WorldClim2 model by Fick and Hijmans (2017). Red dot shows position of the studied core. White dotted square encompasses the zoom shown in Figure 2. B/ Geologic map simplified from Roig et al. (2012).

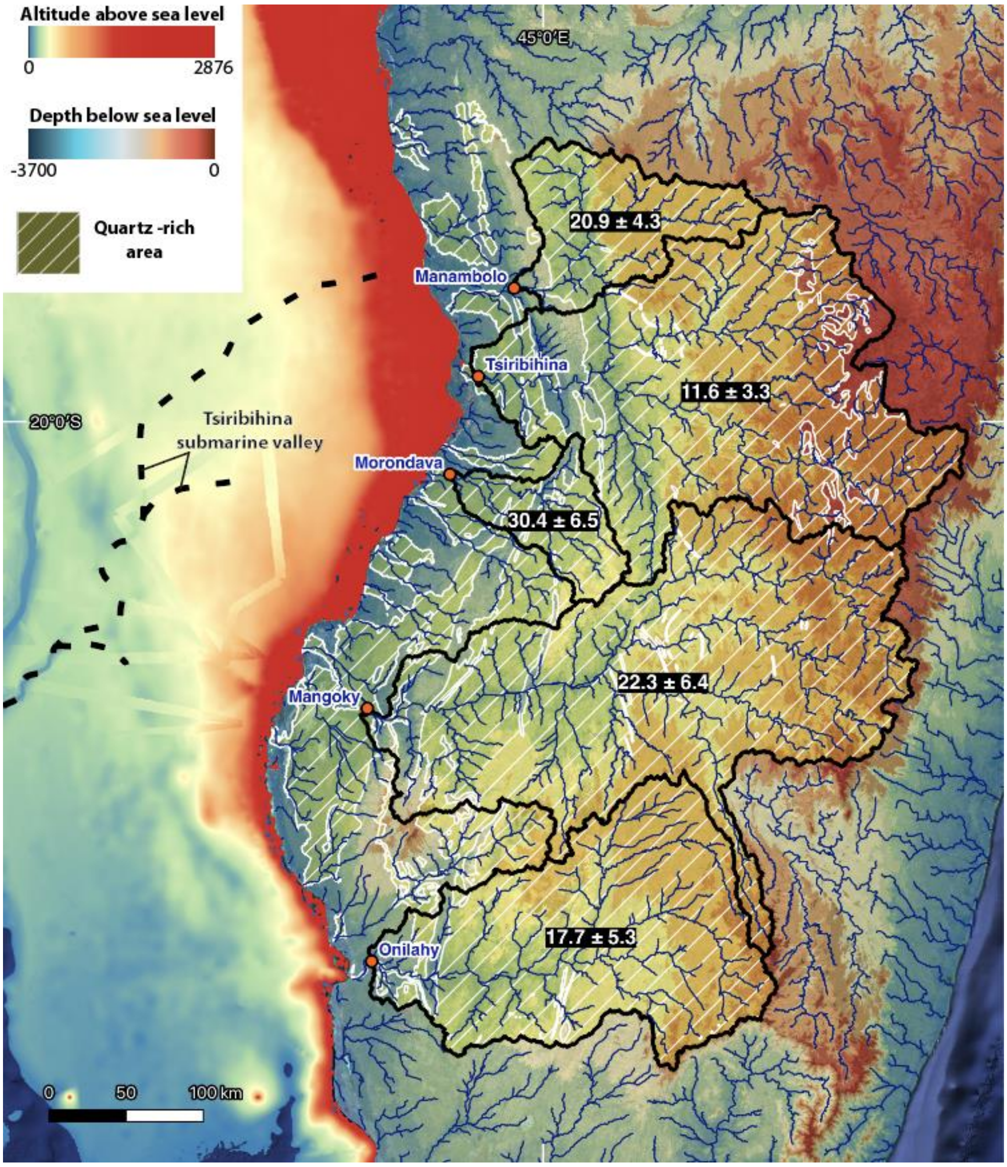

Figure 2 : Catchments delivering sediments to the MOZ4-CS24 core. Red points indicate sites of the five fluvial samples analyzed for heavy minerals, εNd and ^{10}Be measurements were made. ^{10}Be-derived denudation rates for each basin are outlined in yellow. Blue outlined names are towns. The area highlighted in yellow is the quartz rich area. MOZ4-CS24 core and Tsiribihina submarine valley are indicated by a red point and the black dashed line respectively. General bathymetry from GEBCO 2014 Grid (https://www.gebco.net). Higher precision bathymetry lines are from the PAMELA oceanic campaign (Jouet and Deville, 2015).

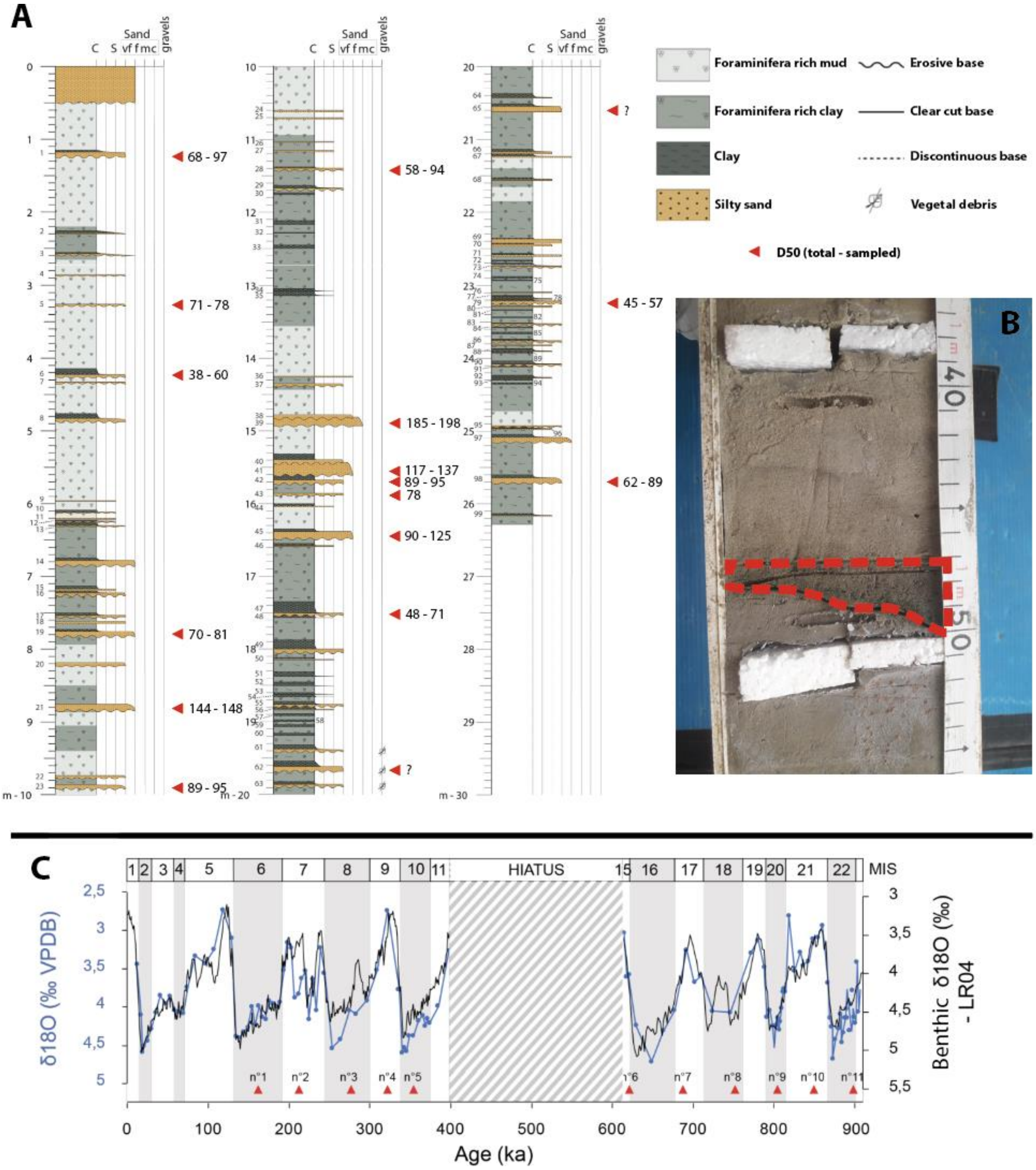

Figure 3 : Stratigraphy and age model of the MOZ4-CS24 core. A/ Log of the MOZ4-CS24 core with sampled intervals indicated by the triangles (adjacent numbers indicate median grain size of the turbidite bed and of specifically sampled portion; for two turbidites indicated by a question mark, the granulometry was not determined. B/ Photo of turbidite layer (indicated by red dashed line) before sampling. C/ Age model for core MOZ4-CS24. Blue and black lines are $\partial^{18}O$ measurements of benthic foraminifera from core MOZ4-CS24 (Sup Info 2 for raw data) and LR04 benthic stack (Lisiecki and Raymo, 2005c). Red triangles indicate calcareous nannofossil samples used for biostratigraphic control of the $\partial^{18}O$-derived age model.

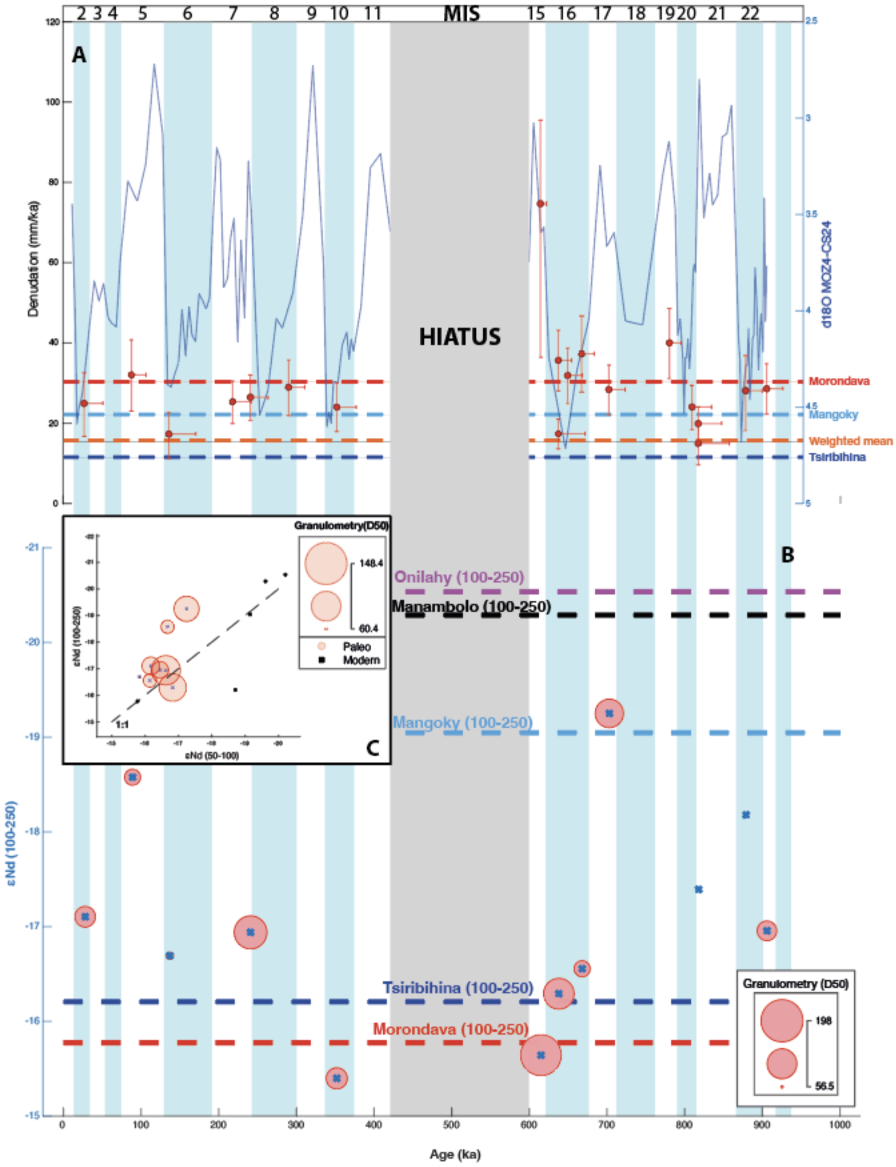

Figure 4 : ^{10}Be derived denudation rates compared to climatic cyclicity and εNd data. In A/ and B/, light blue rectangles represent glacial periods and white areas interglacial periods. Dark grey area represents the hiatus between 400 and 600 ka. A/ Red points represent ^{10}Be-derived denudation rates of the MOZ4-CS24 core in mm/ka. Ages of these points have been shifted 6 ka to the right (explanation provided in text) and age uncertainty represents integration times associated with measured denudation rates (Table 1). Blue curve are benthic ∂^{18}O values from core MOZ4-CS24. Colored dashed lines are denudation rates for modern Mangoky, Tsiribihina and Morondava (highest rates measured for the latter) and weighted mean of all rivers. B/ εNd signatures through MOZ4-CS24 core, compared to signatures of modern rivers of Madagascar. εNd signatures of 100-250 µm sieved samples of core MOZ4-CS24 are shown by blue crosses. Diameter of red circle around each point is proportional to grain size of the sampled turbidite before sieving. Note the granulometry of point S21 at 818 ka was not measured. Dashed colored lines correspond to the signatures of modern rivers. C/ Comparison of εNd for 50 – 100 µm and 100 – 250 µm, when data was available for both fractions.

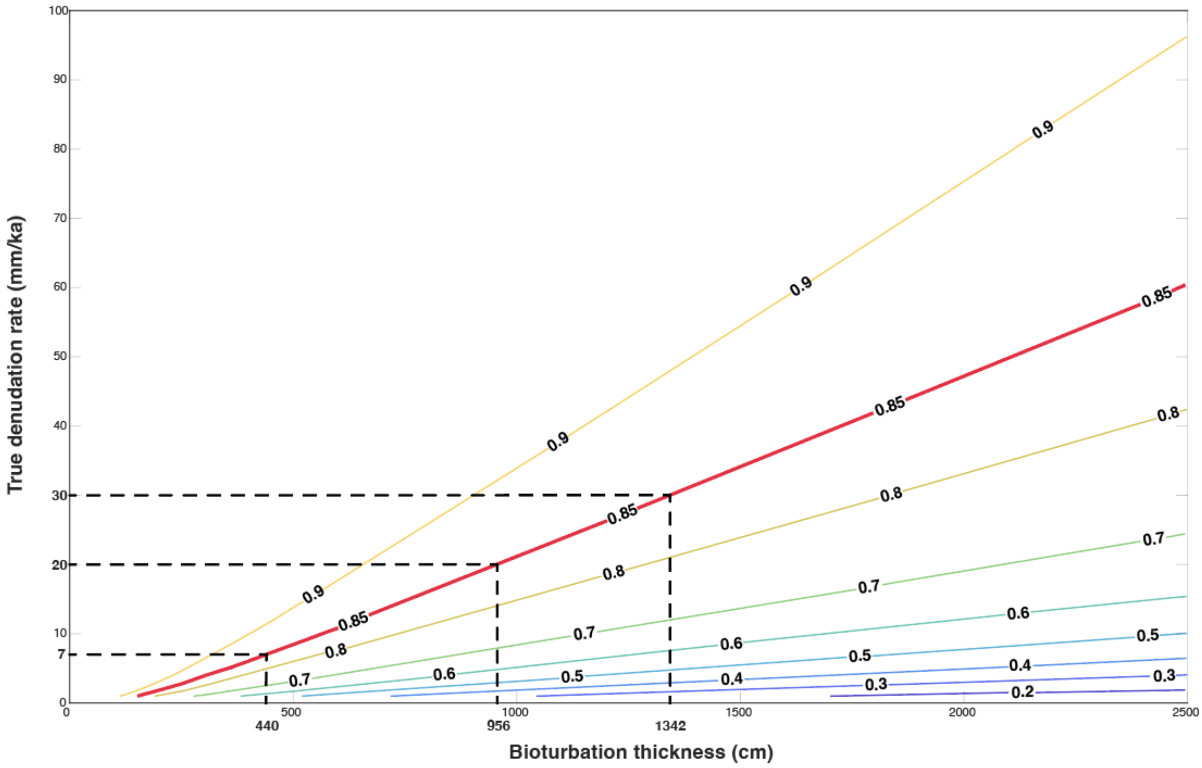

Figure 5 : Variation in measured ^{10}Be ratio with or without bioturbation for different denudation rates and bioturbation thicknesses. Colored lines represent ratios of concentrations measured with bioturbation, relative to a case without bioturbation.

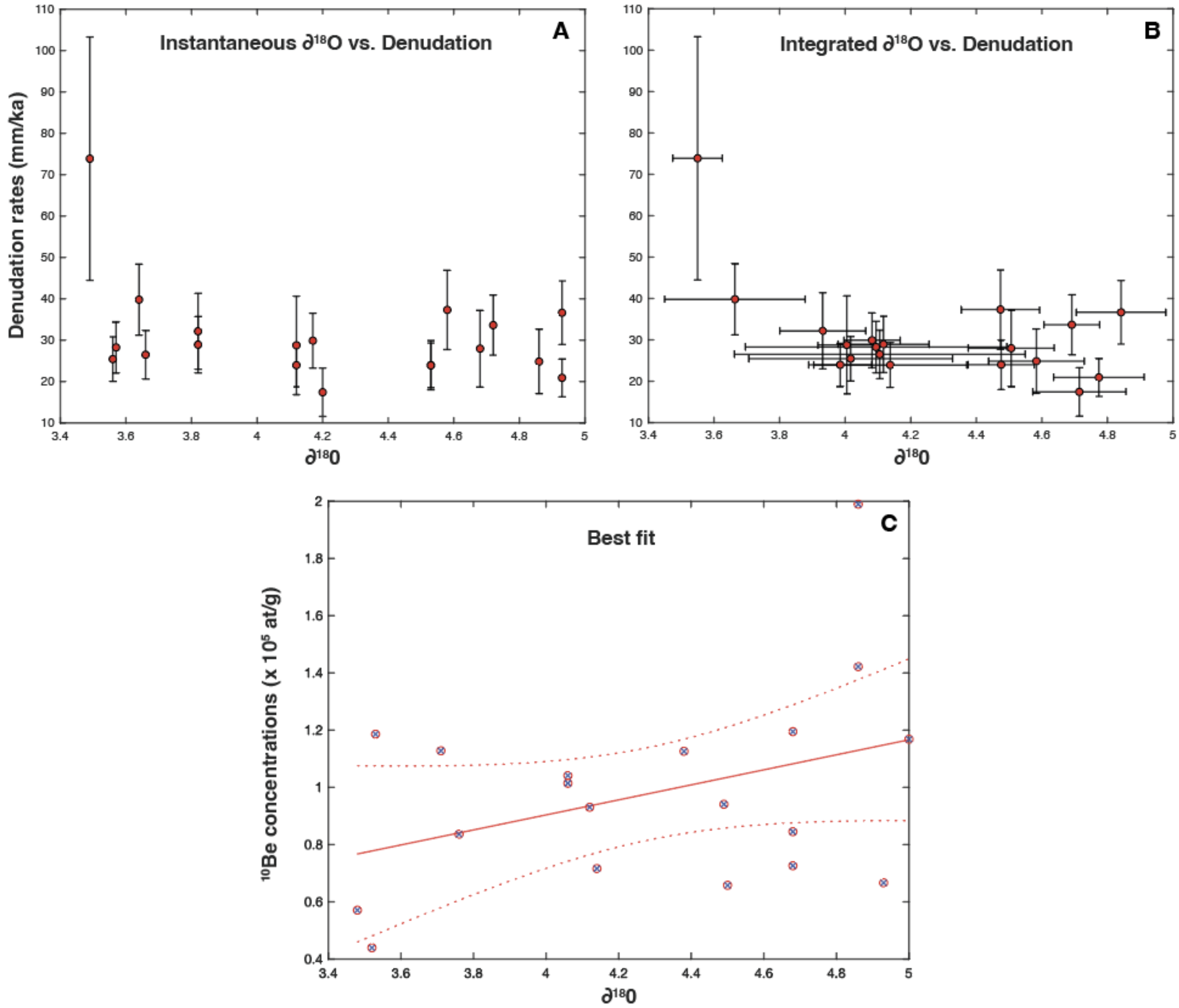

Figure 6 : Comparison of ^{10}Be and ∂^{18}O. A/ ∂^{18}O of the age of deposition of turbidites according to the core's age model versus ^{10}Be-derived denudation rates. B/ mean ∂^{18}O integrated over the integration time associated with each ^{10}Be denudation rate versus ^{10}Be-derived denudation rates. C/ best possible fit between ^{10}Be concentrations and the range of values of ∂^{18}O over each integration time.

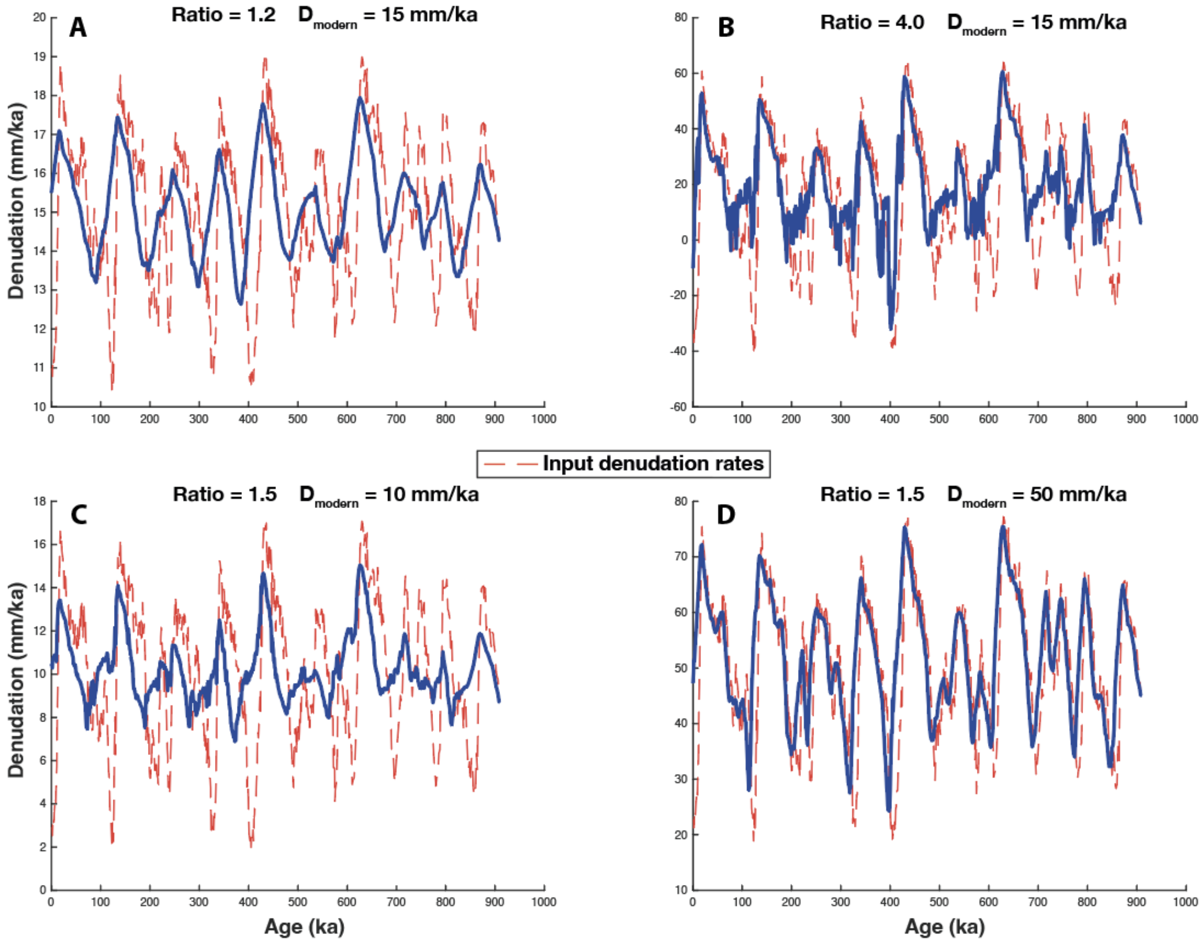

Figure 7 : Sensitivity test of ^{10}Be-derived denudation rates to variations in "true" denudation rates. In each of the graphs, red dotted line represents D_{input} and the plain blue line D_{output}. For each graph, fixed amplitudes of variations and original modern value of denudation are given by the ratios D_{input}/D_{modern} and D_{modern}. Note that denudation rates are negative for graph B. This is an artefact of the model, because we fix the amplitude (1.5) for low denudation rates (15 mm/ka).

Tables

Table 1 : Descriptive table of the MOZ4-CS24 turbiditic data. The core was drilled at 3090 depth below sea level, at 21°31’6.42”S, 45°51’40.475”E. Production rates of quartz-rich areas were used to calculate denudation rates (4.79824 at/g/a for neutrons, 0.014956 at/g/a for slow muons and 0.041427 at/g/a for fast muons). Ages correspond to the age model from the core + 6 ka (explanations provided in text). Corrected ^{10}Be values correspond to the Measured ^{10}Be values corrected for radioactive decay. Uncertainties are 1 sigma.

Core Section	Granulometric fraction	Batch	$^{10}Be/^{9}Be$	^{10}Be Counts	^{9}Be	Mass of Quartz	Measured ^{10}Be	Age	Corrected ^{10}Be	Denudation	Integration time	Denudation
	µm		10^{-15}		10^{19} at	g	10^{4} at/g	ka	10^{4} at/g	mm/ka	ka	t/km^2/a
S2 123-130	50-250	3_4	4.6 ± 0.9	40	3.0	0.8	14.2 ± 3.5	28	14.4 ± 3.5	24.9 ± 7.8	24.1	65.9 ± 20.6
S4 328-330	50-250	3_4	3.8 ± 0.5	64	3.0	0.9	10.4 ± 2.0	89	10.9 ± 2.1	32.2 ± 9.2	18.6	85.3 ± 24.3
S5 420-423	50-250	3_4	3.5 ± 0.6	51	3.0	0.4	19.9 ± 5.3	136	21.3 ± 5.7	17.4 ± 5.8	34.4	46.2 ± 15.5
S8 778-781	50-250	3_4	17.6 ± 0.9	413	3.0	4.2	11.9 ± 0.7	218	13.2 ± 0.8	25.5 ± 5.3	23.6	67.5 ± 14.3
S9 878-882	50-250	3_4	10.6 ± 0.7	275	3.0	2.6	11.3 ± 0.9	241	12.7 ±1.0	26.5 ± 5.9	22.6	70.2 ± 15.6
S10 991-992	50-250	3_4	8.4 ± 0.9	144	3.0	2.3	10.1 ±1.3	291	11.7 ±1.5	28.9 ± 6.8	20.7	76.7 ± 18.1
S12 1142-1143	50-250	3_4	4.7 ± 0.5	109	3.0	1.0	11.9 ±1.8	353	14.3 ± 2.1	24.0 ± 6.0	25.0	63.6 ± 15.8
S15 1488-1490	50-250	3_4	8.5 ± 3.2	11	3.0	5.3	4.4 ± 1.8	615	6.0 ±2.5	73.9 ± 29.4	8.1	195.8 ± 77.9
S16 1559-1562	50-100	1	17.0 ±0.9	392	3.1	3.4	11.7 ± 0.9	637	16.1 ± 1.3	20.9 ± 4.6	28.7	55.4 ± 12.2
S16 1559-1562	100-250	2	19.6 ± 1.0	425	3.1	8.01	6.7 ± 0.4	637	9.2 ± 0.6	36.7 ± 7.7	16.4	97.1 ± 20.4
S16 1570-1572	50-100	2	13.3 ± 0.9	252	3.1	4.7	7.3 ± 0.6	650	10.0 ± 0.8	33.7 ± 7.2	17.8	89.2 ± 19.2
S16 1587-1589	50-250	3_4	4.6 ± 0.5	118	3.0	1.7	6.6 ± 1.0	668	9.2 ± 1.4	37.3 ± 9.6	16.1	99.0 ± 25.4
S17 1647-1650	50-250	3_4	7.9 ± 0.5	239	3.0	2.6	8.4 ± 0.7	706	11.9 ± 1.1	28.3 ± 6.2	21.2	74.9 ± 16.5
S18 1752-1755	50-250	3_4	10.1 ± 0.6	252	3.0	4.9	5.7 ±0.5	781	8.4 ± 0.7	39.8 ± 8.6	15.1	105.5 ± 22.8
S21 1968-1970	50-250	3_4	6.9 ± 0.5	161	3.0	1.9	9.4 ± 1.0	810	14.1 ± 1.5	23.9 ± 5.4	25.1	63.4 ± 14.4
S21 2060-2062	50-100	1	17.0 ± 0.8	432	3.1	4.3	9.3 ± 0.7	818	14.0 ±1.1	24.0 ± 5.2	25.0	63.5 ± 13.7
S21 2060-2062	100-250	2	3.4 ± 0.4	77	3.1	0.33	11.3 ± 5.1	818	16.9 ± 7.6	28.8 ± 11.9	20.8	76.3 ± 31.5
S24 2322-2325	50-250	3_4	2.6 ± 0.3	79	3.0	0.6	8.5 ± 2.3	879	13.1 ± 3.5	28.0 ± 9.3	21.4	74.1 ± 24.6
S26 2568-2570	50-100	2	14.2 ± 1.0	205	3.1	5.2	7.2 ± 0.6	906	11.3 ± 1.0	29.9 ± 6.6	20.1	79.2 ± 17.6

Table 2 : Location, production rates and size of drainage areas of the five modern-river sand samples, used for both ^{10}Be and εNd measurements.

River	Sampling Site	Latitude	Longitude	Elevation	Neutronic production	Fast muonic production	Slow muonic production	Drainage
				m	at/g/a	10^{-2} at/g/a	10^{-2} at/g/a	10^{3} km^{2}
Tsiribihina	Belon'i Tsiribihina	S 19° 42’ 36,6’’	E 044° 35’ 02,7’’	5	5.5	4.4	1.6	47.6
Mangoky	Tanambao	S 21° 50’ 01,9’’	E 043° 52’ 22,4’’	46	5.2	4.2	1.6	53.0
Onilahy	Ambohimahavelona	S 23° 27’ 10,1’’	E 043° 53’ 59,8’’	29	5.0	4.2	1.5	32.0
Manambolo	Bekopaka	S 19° 08’ 40,8’’	E 044° 48’ 49,2’’	46	4.3	4.1	1.5	11.6
Morondava	Upstream Bosimavo	S 20° 20’ 30,9’’	E 044° 24’ 07,1’’	18	3.5	3.9	1.3	6.2

Table 3 : Measured Be ratios for five modern-rivers with associated concentrations, denudation and outflow. Denudation shown in t/km²/a was calculated by multiplying denudation in mm/ka by quartz density (2.65 g/cm³). Outflow was calculated by multiplying denudation in t/km²/a by drainage areas given in Table2. Integration time was calculated considering a production depth of 60 cm. All samples were prepared in two consecutive batches (batches 5_6 of Table 4).

River	Granulometric fraction	$^{10}Be/^{9}Be$	^{10}Be Counts	^{9}Be	Mass of Quartz	Measured 10Be	Denudation	Integration time	Denudation	Outflow
	µm	10^{-14}		10^{19} at	g	10^{4} at/g	mm/ka	ka	t/km^{2}/a	10^{5} t/a
Tsiribihina	50-250	8.7 ± 0.3	1246	2.9	7.4	34.1 ± 1.1	11.2 ± 2.3	53.5	29.7 ± 6.1	14.2 ± 2.9
Tsiribihina	100-700	21.6 ± 0.6	1651	3.0	20.1	31.8 ± 0.9	12.0 ± 2.4	50.1	31.8 ± 6.4	15.1 ± 3.1
Mangoky	50-250	10.6 ± 0.3	1230	3.0	18.3	17.1 ± 0.5	21.1 ± 4.4	28.4	55.9 ± 11.6	30.0 ± 6.1
Mangoky	100-700	9.2 ± 0.3	1255	3.0	17.8	15.3 ± 0.5	23.7 ± 4.9	25.4	62.7 ± 13.0	33.3 ± 6.9
Onilahy	50-250	5.9 ± 0.2	966	3.0	7.6	22.9 ± 0.8	15.1 ± 3.1	39.6	40.1 ± 8.2	12.8 ± 2.6
Onilahy	100-700	10.0 ± 0.5	833	3.0	21.7	13.6 ± 0.6	25.7 ± 5.4	23.3	68.1 ± 14.4	21.8 ± 4.6
Manambolo	100-700	6.8 ± 0.2	1225	3.0	13.8	14.5 ± 0.5	20.9 ± 4.3	28.8	55.3 ± 11.5	6.4 ± 1.3
Morondava	100-700	5.9 ± 0.4	595	3.0	21.1	8.3 ± 0.6	30.4 ± 6.5	19.8	80.5 ± 17.2	5.0 ± 1.1

Table 4 : Values of $^{10}Be/^{9}Be$ ratios of blanks of batches prepared in old CRPG Be lab (batch 1) at CEREGE (batch 2) and at the new clean CRPG lab (batches 3 to 6).

	$^{10}Be/^{9}Be$ 10^{-16}	Total counts	^{9}Be 10^{19} at	^{9}Be Spike ppm
Batch 1	42.0 ± 5.1	74	3.1	2020 ± 6
Batch 2	22.0 ± 3.8	40	3.0	3025 ± 9
Batch 3_4	9.3 ± 1.9	25	3.0	2129 ± 13
	11.8 ± 2.6	25	3.0	
	5.7 ± 2.1	9	3.0	
	6.7 ± 2.1	11	3.0	
Batch 5_6	4.0 ± 1.4	8	3.0	2129 ± 13
	4.0 ± 1.4	9	3.0	
	1.7 ± 1.3	2	2.9	
	6.0 ± 1.8	13	3.7	

Table 5 : Nd isotope measurements (εNd) for separate detrital fractions of core MOZ4-CS24 (first part and modern river sands (second part). Sampling sites are indicated in text and in Table 1 for core MOZ4-CS24 and in Table 2 for modern rivers. Data were normalized to CHUR value of $^{143}Nd/^{144}Nd$ = 0.51263 (Bouvier et al. 2008).

Sample	Granulometry µm	$^{143}Nd/^{144}Nd$ ± (2se 10^{-6})	εNd ± 2se
S2_123-120	50-100	0.511791 ± 13	-16.2 ± 0.3
S2_123-120	100-250	0.511743 ± 14	-17.1 ± 0.4
S4_328-330	50-100	0.511765 ± 16	-16.7 ± 0.4
S4_328-330	100-250	0.511667 ± 14	-18.6 ± 0.4
S5_420-423	50-100	0.511808 ± 18	-15.8 ± 0.4
S5_420-423	100-250	0.511764 ± 14	-16.7 ± 0.3
S8_778-781	50-100	0.511802 ± 19	-16.0 ± 0.4
S9_878-882	50-100	0.511768 ± 12	-16.6 ± 0.3
S9_878-882	100-250	0.511751 ± 16	-16.9 ± 0.4
S12_1142-1143	100-250	0.511830 ± 16	-15.4 ± 0.4
S15_1488-1490	100-250	0.511818 ± 13	-15.6 ± 0.3
S16_1559-1562	50-100	0.511757 ± 14	-16.8 ± 0.3
S16_1559-1562	100-250	0.511785 ± 13	-16.3 ± 0.3
S16_1570-1572	50-100	0.511764 ± 18	-16.7 ± 0.4
S16_1587-1589	50-100	0.511792 ± 14	-16.1 ± 0.3
S16_1587-1589	100-250	0.511771 ± 11	-16.6 ± 0.3
S17_1647-1650	50-100	0.511736 ± 25	-17.2 ± 0.5
S17_1647-1650	100-250	0.511633 ± 23	-19.3 ± 0.5
S18_1752-1755	50-100	0.511702 ± 24	-17.9 ± 0.5
S21_2060-2062	100-250	0.511728 ±13	-17.4 ± 0.3
S24_2322-2325	100-250	0.511688 ± 18	-18.2 ± 0.4
S26_2568-2570	50-100	0.511776 ± 17	-16.5 ± 0.4
S26_2568-2570	100-250	0.511751 ± 14	-17.0 ± 0.3
Tsiribihina	50-100	0.511661 ± 8	-18.7 ± 0.3
Tsiribihina	100-250	0.511789 ± 8	-16.2 ± 0.3
Manambolo	50-100	0.511615 ± 9	-19.6 ± 0.3
Manambolo	100-250	0.511580 ± 6	-20.3 ± 0.2
Morondava	50-100	0.511811 ± 8	-15.8 ± 0.3
Morondava	100-250	0.511811 ± 8	-15.8 ± 0.3
Mangoky	50-100	0.511638 ± 9	-19.1 ± 0.3
Mangoky	100-250	0.511643 ± 8	-19.0 ± 0.3
Onilahy	50-100	0.511584 ± 6	-20.2 ± 0.2
Onilahy	100-250	0.511567 ± 6	-20.5 ± 0.2

Table 6 : Transparent heavy-mineral assemblages in studied Tsiribihina Valley samples. Estimated contribution of Mangoky river sediment for each sample is indicated in last column (the rest is inferred to have been supplied in subequal proportions from Tsiribihina and Manambolo rivers debouching north of submarine Tsiribihina Valley.

Sample	Age (ka)	HMC	tHMC	zircon	tourmaline	rutile	anatase	titanite	apatite	monazite	epidote	garnet	staurolite	kyanite	sillimanite	amphibole	clinopyroxene	hypersthene	other tHM	ZTR	ACI	MMI	Sil.I.	Est. Mangoky supply
S2 123-120	22	3.0	2.1	4	3	2	2	1	1	0	6	9	0	0	5	62	2	2	0	10	13	100	90	0.64
S4 328-330	83	3.3	2.1	7	1	0.4	3	2	3	0	7	11	0	2	7	52	4	0.4	0	8	16	90	100	0.80
S5 420-423	131	2.5	1.5	8	4	1	0.5	3	3	1	7	12	0	0.5	1	54	3	1	0	14	9	88	n.d.	0.77
S8 778-781	213	3.7	2.0	4	2	1	1	3	1	0	4	5	0	1	1	69	4	1	0.5	8	16	75	n.d.	0.39
S9878-882	236	1.9	1.0	6	4	0.4	0.4	3	2	3	5	19	0	0.4	5	46	4	1	1	11	32	96	100	0.98
S10 991-992	285	3.0	1.4	8	4	1	3	1	4	1	3	13	0	1	6	52	5	0.5	0	13	16	92	100	0.80
S12 1142-1143	347	5.2	2.6	7	5	1	1	2	2	1	8	5	0	0	1	62	3	1	0.5	13	15	n.d.	n.d.	0.53
S15 1488-1490	609	2.2	1.3	3	2	2	1	0.5	2	0.5	6	17	0.5	1	4	53	4	1	0	7	25	85	100	0.88
S16c 1559-1562	632	3.4	1.9	7	2	1	1	2	2	1	2	10	1	0	3	65	2	0	1	10	15	88	100	0.60
S16b 1570-1572	644	3.9	2.1	6	4	1	5	3	4	0..5	6	6	0	0	4	55	3	0.5	1	12	15	100	100	0.65
S16a 1587-1589	662	2.3	1.2	8	6	2	3	2	4	0.5	2	13	1	0.5	1	52	4	0	0	16	13	75	n.d.	0.79
S17 1647-1650	670	2.1	1.2	5	3	0.5	0.5	3	2	0	7	1	0	0.5	0.5	73	1	1	0.5	9	12	n.d.	n.d.	0.30
S18 1752-1755	775	4.0	2.4	2	2	0.5	2	3	5	0.5	3	9	1	0	4	62	2	1	0	5	14	90	100	0.62
S20 1968-1970	804	4.0	1.9	5	4	2	2	1	4	0	6	10	0.5	1	4	57	4	0	0	11	25	88	100	0.71
S21 2060-2062	812	7.4	3.4	5	4	0	0.5	1	6	0	4	5	0	0.5	4	59	9	1	0	9	28	94	100	0.50
S24 2322-2325	873	4.3	2.0	1	5	0.5	4	2	2	0.5	7	3	0	0	2	67	2	0.5	1	7	13	100	100	0.43
S26 2568-2570	900	4.7	3.0	1	3	0	1	2	2	0.5	2	9	0	1	1	71	4	0.5	0	5	24	70	n.d.	0.48

Supplementary material

Age model of the MOZ4-CS24 core

MIS 5, 6, 9 and 10 where easily identifiable by correlation of the benthic ∂^{18}O record of core MOZ4-CS24 and the LR04 benthic stack. Correlations were fixed to glacial and interglacial transitions using the *Analyseries* software (Paillard et al., 1996). Nannofossil-based biostratigraphic analyses confirmed the ∂^{18}O-based age model from MIS1 to 10 and constrained the age model for the bottom half of the core by introducing a hiatus from Mis 11 to MIS 15. MIS 9 to MIS 11 were validated from samples 4 and 5 (Fig. 3C), by the presence of a *Gephyrocapsa caribbeanica* acme zone and the absence of *Pseudoemiliania lacunosa*. The presence in sample 6 of *P. lacunosa*, together with a mixed dominance of *G. carribeanica* and small *Gephyrocapsa*, as well as the absence *Reticulofenestra asanoi* and *Helicosphaera sellii*, allows to constrain the stratigraphic range of the hiatus.

Sup. Info. 1 : Calcareous nannofossil stratigraphy (after Di Stefano et al., 2023; Giraudeau et al., 1998). Location of samples on the core are given in figure 3C.

Sample	Depth (cm)	Observations	Period
1	548	Small *Gephyrocapsa*; presence of *E. huxleyi*	MIS 6 - 8
2	768		
3	970	Transition from small *Gephyrocapsa* / *G. carribbeanica*; absence of *E. huxleyi* and *P. lacunosa*	Transition MIS 8/9
4	1045	Acme *Gephyrocapsa carribbeanica*; absence of *P. lacunosa*	MIS 9 - 11
5	1185		
6	1470	Transition from acme *G. carribbeanica* / *small Gephyrocapsa*; presence of *P. lacunosa*; absence of *R. asanoi* and *H. sellii*. Reworked	MIS15 - 16
7	1548	Acme Small *Gephyrocapsa*; presence of *P. lacunosa*; absence of *R. asanoi* and *H. sellii*. Less reworked than above	MIS 15 - 23
8	1637		
9	1900	Acme Small Gephyrocapsa; presence of P. lacunosa; absence of R. asanoi and H. sellii	MIS 15 - 23
10	2135		
11	2495		

Sup. Info. 2 : Benthic $\partial^{18}O$ values (‰ VPDB) of core MOZ4-CS24 and associated position on the core and age.

Top (cm)	65	85	95	105	125	145	165	185	205	225	245	265	290	305	323	345	365	385	405	425	445	465	488
∂18O (‰ VPDB)	3.444	4.097	4.588	4.509	4.437	4.291	4.07	3.845	3.949	3.859	4.035	4.064	4.083	3.738	3.327	3.432	3.238	2.72	3.086	4.382	4.395	4.332	4.27
Age (ka)	11.6	15.8	18.0	20.1	24.4	28.6	34.2	40.1	46.1	52.1	57.8	62.5	68.4	73.5	83.4	95.4	106.3	117.2	128.2	134.3	138.8	143.3	148.5

Top (cm)	508	528	548	565	585	605	625	645	665	685	706	726	746	768	785	805	826	845	865	887	907	927	946
∂18O (‰ VPDB)	3.991	4.234	3.979	4.127	4.159	3.912	3.945	3.991	3.933	3.511	3.154	3.215	3.879	3.831	3.622	3.52	4.162	3.632	4.036	3.223	3.554	4.542	4.417
Age (ka)	153.0	157.5	162.0	165.9	170.4	174.9	179.4	183.9	188.4	192.9	197.6	202.1	206.6	211.6	215.4	219.9	224.6	228.9	233.4	238.3	242.8	252.8	263.3

Top (cm)	966	980	1005	1025	1045	1066	1085	1105	1124	1145	1185	1224	1264	1285	1304	1325	1345	1364	1385	1405	1449	1470	1505
∂18O (‰ VPDB)	4.04	4.089	3.905	3.51	2.728	3.765	4.603	4.528	4.584	4.367	4.372	4.177	4.111	4.252	4.148	4.21	3.978	3.257	3.185	3.587	3.746	3.019	3.595
Age (ka)	274.3	282.0	295.7	308.1	321.3	335.1	339.2	342.1	344.8	347.8	353.5	359.1	364.9	367.9	370.6	373.6	383.3	395.2	408.3	420.8	599.3	605.3	614.5

Top (cm)	1520	1535	1564	1584	1605	1625	1637	1650	1665	1685	1725	1745	1765	1785	1824	1868	1886	1907	1926	1949	1972	1992	2012
∂18O (‰ VPDB)	3.565	4.243	4.715	4.311	4.044	3.245	3.666	3.594	4.053	4.073	3.294	3.119	3.471	4.127	4.042	4.254	4.531	4.245	4.241	4.144	4.302	4.192	4.009
Age (ka)	618.4	624.9	646.2	660.9	676.3	690.8	699.4	708.78	723.4	745.4	771.4	779.4	787.4	790.7	793.8	797.3	798.8	800.4	802.0	803.8	805.6	807.2	808.9

Top (cm)	2032	2049	2070	2090	2110	2135	2148	2170	2190	2210	2230	2250	2278	2297	2311	2336	2368	2385	2400	2415	2431	2450	2465
∂18O (‰ VPDB)	3.8	3.76	3.799	2.8	3.519	3.282	3.45	3.4	3.097	3.08	2.933	3.683	4.136	4.262	4.683	4.422	4.283	4.283	4.094	4.46	4.339	4.142	4.125
Age (ka)	810.5	811.8	813.5	818.3	824.2	831.6	835.5	842.0	847.9	853.8	859.7	865.7	868.8	870.8	872.3	874.9	878.3	880.1	881.7	883.3	885.0	887.0	888.6

Top (cm)	2479	2498	2521	2535	2551	2575	2590	2605	2620
∂18O (‰ VPDB)	3.777	3.957	4.307	4.14	4.017	4.214	3.414	4.055	3.767
Age (ka)	890.1	892.1	894.6	896.1	897.8	900.3	901.9	903.5	905.1

Sup. Info. 3 : Correlation pointers : benthic $\partial^{18}O$ from MOZ4-CS24 aligned to LR04.

MOZ4-CS24 depth (cm)	MOZ4-CS24 age LR04 (ky)
75.4	13.8
150.1	29.7
241.5	57
299.9	70.8
410.1	131
678	191.3
910	243.5
1012.1	299.7
1068.7	336.9
1330.9	374.4
1405.3	421
1449.1	599.7
1529.8	621
1606.3	677.3
1654.9	712.3
1699.1	761
1770	789.5
2075.3	813.9
2250.7	865.9
2580.9	900.9

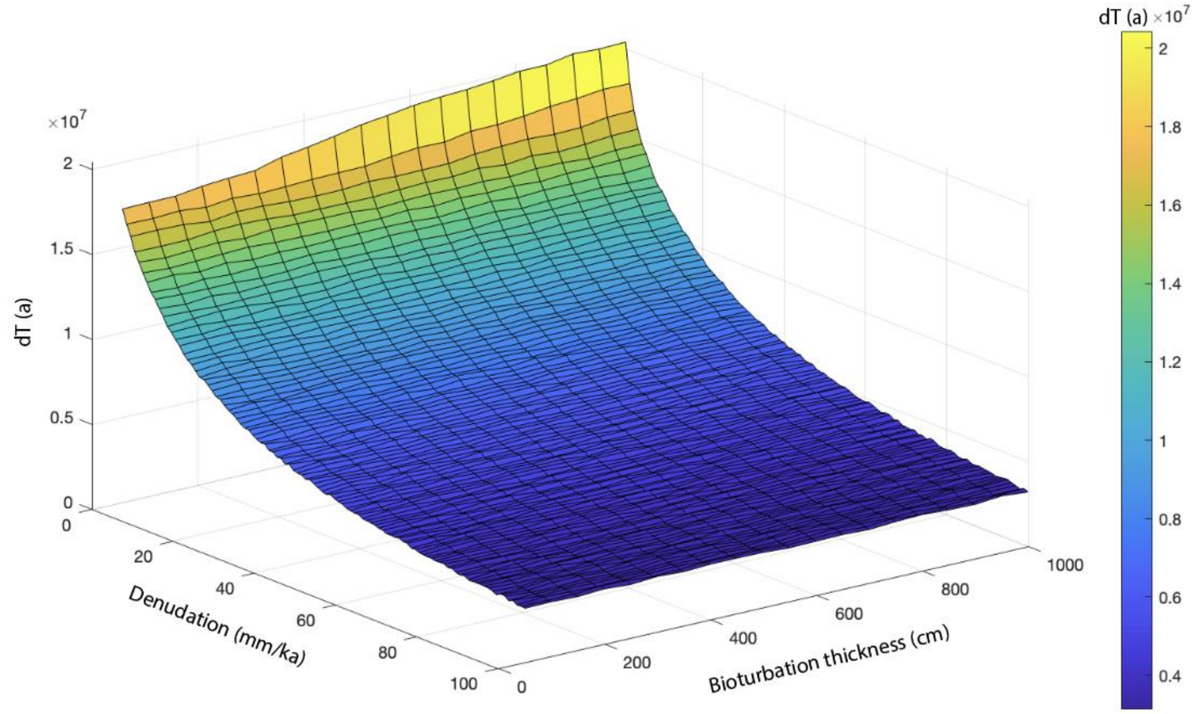

Sup. Info. 4 : Time differences (dT) to reach steady state in conditions with and without bioturbation depending on denudation (mm/ka) and bioturbation thickness (cm). See text for further details

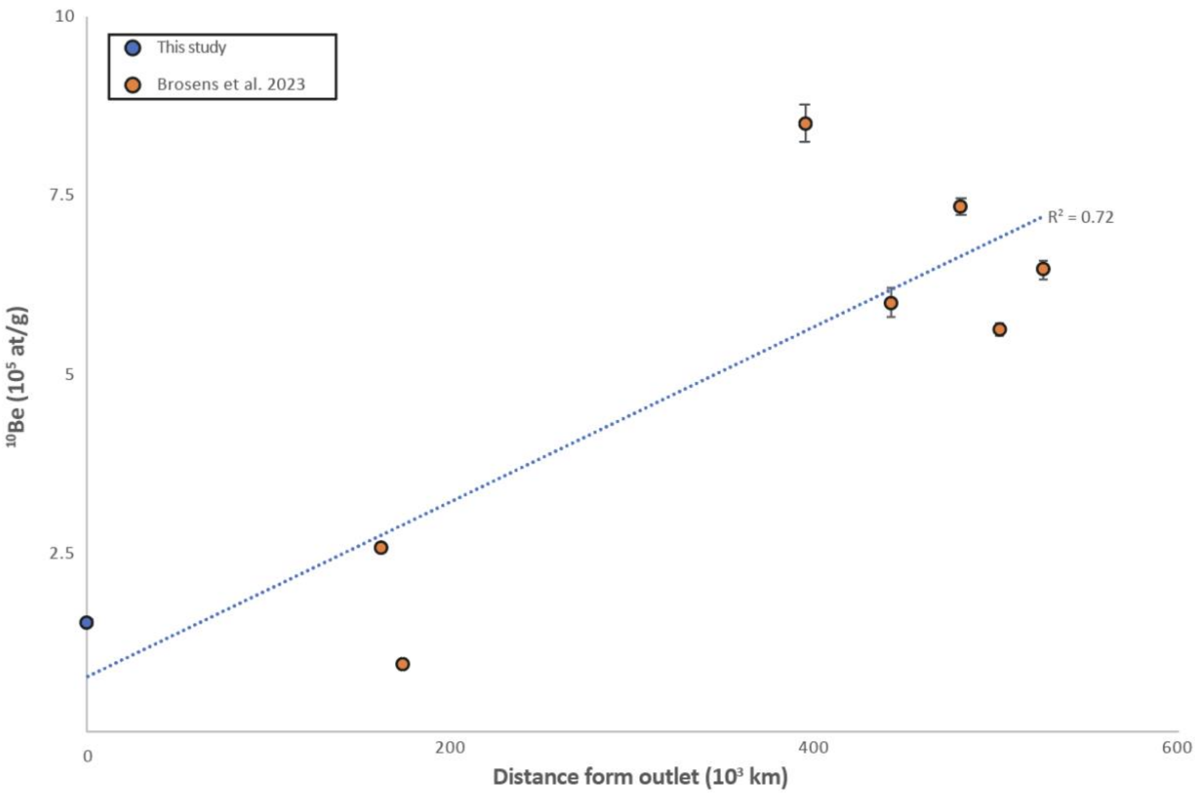

Sup. Info. 5 : ^{10}Be oncentration of the Mangoky river Madagascar as a function of distance from the downstream most sampling point. Blue point is from this study (Table 3). The 100-700 µm was used. Orange points correspond to data from Brosens et al., 2023. The data points are, from downstream to upstream : 2011-11; 2011-12; 2011-08; MDG-1199B1; 2011-07; 2011-26; 2011-25.

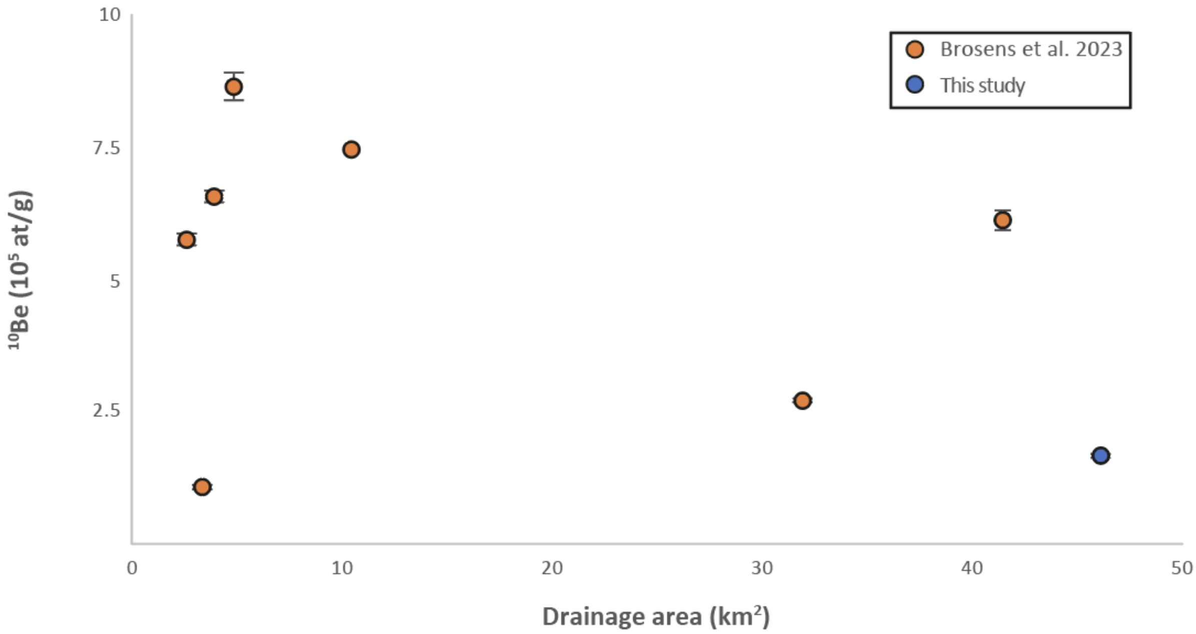

Sup. Info. 6 : ^{10}Be concentrations as a function of drainage area. The data points are the same as in Appendix 1.

Sup. Info 7 : Major and Trace elements of Malagasy rivers measured by the SARM (https://sarm.cnrs.fr/index.html/)

River	Granulometry µm	As µg/g	Ba µg/g	Be µg/g	Bi µg/g	Cd µg/g	Co µg/g	Cr µg/g	Cs µg/g	Cu µg/g	Ga µg/g	Ge µg/g	Hf µg/g	In µg/g	Mo µg/g	Nb µg/g	Ni µg/g	Pb µg/g	Rb µg/g	Sb µg/g	Sc µg/g	Sn µg/g	Sr µg/g
Tsiribihina	100-250	< L.D.	883	0.62	< L.D.	0.05	0.25	2.83	0.57	< L.D.	6.84	0.71	7.8	< L.D.	< L.D.	0.48	< L.D.	13.99	63.7	< L.D.	< L.D.	< L.D.	260
Manambolo	50-100	< L.D.	1619	0.97	< L.D.	0.58	0.29	3.54	0.65	< L.D.	11.23	0.79	108.1	< L.D.	< L.D.	1.36	< L.D.	23.55	107.5	0.17	< L.D.	< L.D.	362
Manambolo	100-250	< L.D.	1260	0.67	< L.D.	0.21	0.25	2.54	0.42	< L.D.	8.05	0.71	32.3	< L.D.	< L.D.	1.11	< L.D.	18.73	81.3	0.20	< L.D.	< L.D.	276
Morondava	50-100	< L.D.	911	0.56	< L.D.	0.51	0.56	10.35	0.58	< L.D.	6.46	0.61	122.0	< L.D.	< L.D.	4.71	< L.D.	15.65	69.1	0.20	1.32	< L.D.	191
Morondava	100-250	< L.D.	771	0.28	< L.D.	< L.D.	0.20	4.39	0.44	< L.D.	4.27	0.58	5.4	< L.D.	< L.D.	0.57	< L.D.	12.32	57.5	0.18	< L.D.	< L.D.	132
Mangoky	50-100	< L.D.	1162	1.16	< L.D.	1.08	0.35	9.72	0.94	< L.D.	11.04	0.85	213.8	< L.D.	< L.D.	7.63	< L.D.	24.67	118.2	0.19	2.18	0.63	292
Mangoky	100-250	< L.D.	833	0.57	< L.D.	0.12	0.26	5.54	0.84	4.24	6.87	0.70	24.5	< L.D.	< L.D.	2.27	< L.D.	18.32	97.9	0.19	< L.D.	< L.D.	189
Onilahy	100-250	< L.D.	533	0.47	< L.D.	0.12	0.24	4.84	0.33	< L.D.	5.67	0.71	18.6	< L.D.	< L.D.	1.72	< L.D.	10.62	45.7	0.17	< L.D.	< L.D.	181

River	Granulometry µm	Ta µg/g	Th µg/g	U µg/g	V µg/g	W µg/g	Y µg/g	Zn µg/g	Zr µg/g	La µg/g	Ce µg/g	Pr µg/g	Nd µg/g	Sm µg/g	Eu µg/g	Gd µg/g	Tb µg/g	Dy µg/g	Ho µg/g	Er µg/g	Tm µg/g	Yb µg/g	Lu µg/g
Tsiribihina	100-250	0.14	1.30	0.62	< L.D.	< L.D.	2.59	< L.D.	342	3.76	6.07	0.77	2.75	0.49	0.31	0.42	0.06	0.42	0.10	0.31	0.06	0.46	0.08
Manambolo	50-100	0.14	2.64	3.18	3.19	< L.D.	13.91	< L.D.	4729	2.90	4.71	0.60	2.19	0.53	0.35	0.70	0.17	1.56	0.50	2.02	0.42	4.03	0.72
Manambolo	100-250	0.13	1.33	0.94	2.47	< L.D.	4.82	< L.D.	1436	3.12	5.22	0.62	2.16	0.44	0.30	0.39	0.07	0.61	0.17	0.63	0.13	1.19	0.20
Morondava	50-100	0.46	2.57	4.48	8.49	< L.D.	20.97	< L.D.	5431	3.52	6.31	0.77	2.95	0.82	0.52	1.12	0.28	2.44	0.72	2.68	0.53	4.85	0.79
Morondava	100-250	0.05	0.67	0.37	1.94	< L.D.	2.00	< L.D.	207	3.56	5.75	0.72	2.70	0.48	0.32	0.36	0.05	0.34	0.07	0.23	0.04	0.29	0.05
Mangoky	50-100	0.74	7.81	9.76	12.32	< L.D.	29.58	< L.D.	8863	7.60	12.96	1.49	5.36	1.33	0.87	1.66	0.38	3.51	1.04	3.93	0.80	7.45	1.27
Mangoky	100-250	0.22	1.48	1.38	4.25	< L.D.	4.89	< L.D.	1033	6.09	9.36	1.09	3.86	0.71	0.56	0.59	0.10	0.72	0.18	0.60	0.12	0.99	0.16
Onilahy	100-250	0.16	1.41	0.91	5.20	< L.D.	3.89	< L.D.	785	5.69	8.44	0.91	3.16	0.54	0.51	0.45	0.08	0.56	0.14	0.48	0.09	0.75	0.12

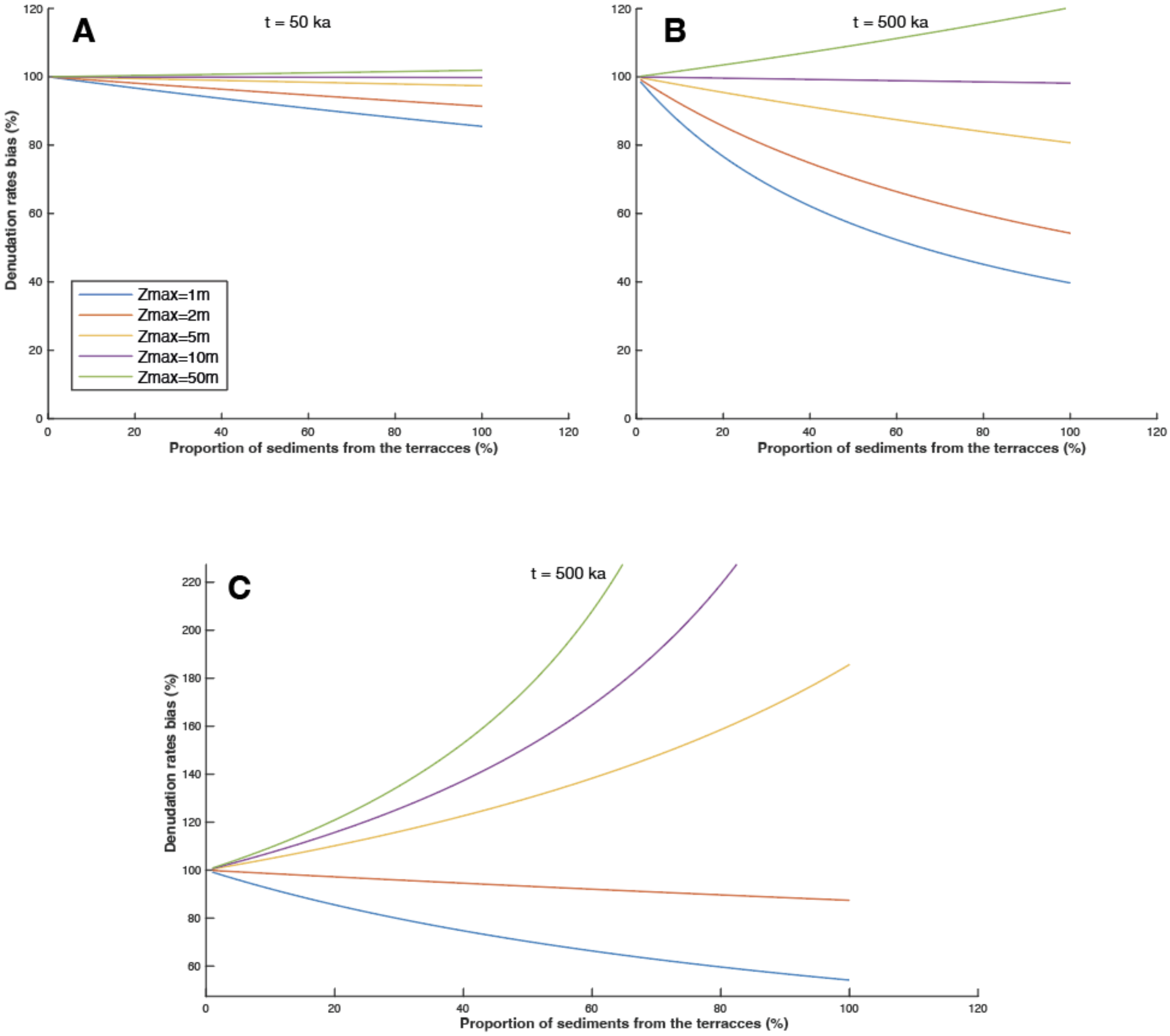

Sup. Info. 8 : Tests of denudation rate bias by the addition of stored material within the river with depleted ^{10}Be concentrations. For all graphs, the true denudation rate is fixed at 6 mm/ka. For each graph, the different colors of the lines represent different thicknesses of the terraces. A/ Bias in the case of addition of different percentages of sediment stored in a terrace of different thicknesses for 50 ka. B/ Same as in A/ but with a storage within the terrace of 500 ka. C/ Addition of sediments to the sample from a terrace with an itintial concentration of 5 x 10^4 at/g (i.e., stronger denudation rates), stored for 500 ka.